

1 **SSWD-EvoEpi: A Coupled Eco-Evolutionary**
2 **Epidemiological Model**
3 **for Sea Star Wasting Disease in *Pycnopodia***
4 ***helianthoides***

5 Technical Report — Model Development and Sensitivity Analysis

6 Willem Weertman^{1,2}

¹Department of Psychology, University of Washington, Seattle, WA

²Friday Harbor Laboratories, University of Washington, Friday Harbor, WA

7 February 21, 2026

8 **Abstract**

9 Sea star wasting disease (SSWD) caused one of the largest wildlife mass mor-
10 tality events in marine ecosystems, driving the sunflower sea star (*Pycnopodia he-*
11 *lianthoides*) to a 90.6% range-wide decline and IUCN Critically Endangered sta-
12 tus. The recent identification of *Vibrio pectenicida* strain FHCF-3 as a causative
13 agent, combined with active captive breeding and the first experimental outplanting
14 of captive-bred juveniles, creates an urgent need for quantitative tools to guide
15 recovery. We present SSWD-EvoEpi, an individual-based, spatially explicit eco-
16 evolutionary epidemiological model coupling *V. pectenicida* transmission dynamics
17 with polygenic host evolution under sweepstakes reproductive success. Each agent
18 carries a diploid genotype across 51 loci governing three fitness-related traits — re-
19 sistance (immune exclusion), tolerance (damage limitation), and recovery (pathogen
20 clearance) — that evolve in response to disease-driven selection. Disease dynamics
21 follow an SEIR compartmental structure with an environmental pathogen reser-
22 voir, pathogen evolution along a virulence—transmission tradeoff, and temperature-
23 dependent forcing. Reproduction implements sweepstakes reproductive success with
24 $N_e/N \sim 10^{-3}$, sex-asymmetric spawning induction, and post-spawning immuno-
25 suppression. Four rounds of global sensitivity analysis (Morris screening and Sobol
26 variance decomposition) across up to 47 parameters reveal that model behavior
27 is dominated by nonlinear interactions among disease mortality rate, host suscep-
28 tibility, environmental pathogen pressure, and genetic architecture, with recovery

29 trait evolution emerging as the fastest adaptive response. The model provides a
30 framework for evaluating captive-bred release strategies, assisted gene flow, and the
31 feasibility of evolutionary rescue on conservation-relevant timescales.

32 Contents

33	1 Introduction	6
34	1.1 Sea Star Wasting Disease and the Collapse of <i>Pycnopodia helianthoides</i>	6
35	1.2 Etiology: A Decade-Long Mystery Resolved	6
36	1.3 Conservation Urgency and Active Recovery Efforts	7
37	1.4 The Need for an Eco-Evolutionary Framework	8
38	1.5 Model Overview	9
39	1.6 Paper Outline	10
40	2 Model Architecture	10
41	2.1 Agent Representation	10
42	2.2 Node Structure	12
43	2.3 Simulation Loop	12
44	2.4 Design Rationale	13
45	3 Disease Module	14
46	3.1 Compartmental Structure	14
47	3.1.1 Erlang-Distributed Stage Durations	15
48	3.2 Force of Infection	15
49	3.2.1 Dose–Response Function	16
50	3.2.2 Salinity Modifier	16
51	3.2.3 Size-Dependent Susceptibility	16
52	3.2.4 Post-Spawning Immunosuppression	17
53	3.3 Disease Progression and Recovery	17
54	3.3.1 Transition Rates	17
55	3.3.2 Temperature Scaling (Arrhenius)	17
56	3.3.3 Tolerance: Extending I_2 Duration	18
57	3.3.4 Recovery	18
58	3.4 Vibrio Dynamics	19
59	3.4.1 Shedding	19
60	3.4.2 Carcass Shedding	19
61	3.4.3 Vibrio Decay	19
62	3.4.4 Environmental Reservoir	20
63	3.5 Pathogen Evolution	20
64	3.5.1 Virulence–Tradeoff Curves	20
65	3.5.2 Transmission and Mutation	21
66	3.6 Basic Reproduction Number	21
67	3.7 Daily Update Sequence	21

68	4 Genetics Module	22
69	4.1 Three-Trait Architecture	22
70	4.2 Trait Score Computation	23
71	4.2.1 Effect Size Distribution	23
72	4.2.2 Coupling to Disease Dynamics	24
73	4.3 Genotype Initialization	24
74	4.4 Mendelian Inheritance and Mutation	25
75	4.5 Sweepstakes Reproductive Success	25
76	4.6 Genetic Diagnostics and Tracking	26
77	4.7 Genotype Bank (Tier 2 Nodes)	27
78	5 Population Dynamics	27
79	5.1 Life Stages	27
80	5.2 Growth	28
81	5.3 Natural Mortality	28
82	5.4 Spawning System	29
83	5.4.1 Spawning Season and Phenology	29
84	5.4.2 Spontaneous Spawning	30
85	5.4.3 Cascade Induction	30
86	5.4.4 Post-Spawning Immunosuppression	31
87	5.5 Fecundity	31
88	5.6 Fertilization Kinetics and the Allee Effect	31
89	5.7 Larval Phase	32
90	5.8 Settlement and Recruitment	32
91	5.9 Continuous Settlement	33
92	5.10 Demographic–Genetic–Epidemiological Coupling	33
93	6 Spatial Module and Environmental Forcing	34
94	6.1 Metapopulation Network Structure	34
95	6.1.1 Node Definition	34
96	6.1.2 Internode Distance Computation	35
97	6.2 Connectivity Matrices	36
98	6.2.1 Larval Connectivity Matrix C	36
99	6.2.2 Pathogen Dispersal Matrix D	36
100	6.2.3 Dispersal Dynamics	37
101	6.3 Environmental Forcing	37
102	6.3.1 Sea Surface Temperature	38
103	6.3.2 Temperature-Dependent Rate Scaling	38
104	6.3.3 Salinity Modifier	39

105	6.3.4 Flushing Rate	39
106	6.4 Agent Movement	40
107	6.5 Network Configurations	40
108	6.5.1 5-Node Validation Network	40
109	6.5.2 11-Node Sensitivity Analysis Network	41
110	6.5.3 Full-Range Network (Planned)	42
111	6.6 Network Construction	42
112	7 Sensitivity Analysis	43
113	7.1 Methods	43
114	7.1.1 Morris Elementary Effects Screening	43
115	7.1.2 Sobol Variance Decomposition	43
116	7.1.3 Output Metrics	44
117	7.2 Progressive Sensitivity Analysis Design	44
118	7.3 Round 4 Morris Results	46
119	7.3.1 Global Parameter Ranking	46
120	7.3.2 Key Rank Shifts from Round 3	47
121	7.3.3 New Three-Trait Parameters	50
122	7.3.4 Universal Nonlinearity	50
123	7.3.5 Module-Level Sensitivity	51
124	7.4 Cross-Round Parameter Trajectories	52
125	7.5 Sobol Variance Decomposition: Rounds 1–2 and Ongoing	53
126	7.5.1 R1–R2 Sobol Results	53
127	7.5.2 Round 4 Sobol (In Progress)	54
128	7.6 Summary and Implications	54
129	8 Validation	59
130	8.1 K = 5,000 Validation	59
131	8.2 K = 100,000 Scale-Up Validation	62
132	8.3 Cross-Scale Comparison	63
133	8.4 Key Scientific Findings	64
134	8.4.1 Evolutionary Rescue Is Insufficient	64
135	8.4.2 Recovery as the Primary Adaptive Pathway	65
136	8.4.3 The Extinction Vortex Persists at Realistic Scales	65
137	8.4.4 Implications for Captive Breeding	66
138	9 Discussion	67
139	A Parameter Tables	73

¹⁴⁰ **1 Introduction**

¹⁴¹ **1.1 Sea Star Wasting Disease and the Collapse of *Pycnopodia***
¹⁴² ***helianthoides***

¹⁴³ Sea star wasting disease (SSWD) caused one of the largest documented wildlife mass
¹⁴⁴ mortality events in marine ecosystems when it swept through populations of over 20
¹⁴⁵ asteroid species along the northeastern Pacific coast beginning in 2013 [23, 29, 47]. The
¹⁴⁶ disease, characterized by behavioral changes (arm twisting, lethargy), loss of turgor,
¹⁴⁷ body wall lesions, ray autotomy, and rapid tissue degradation, devastated populations
¹⁴⁸ from Baja California to the Gulf of Alaska within months [32, 46]. Among the species
¹⁴⁹ affected, the sunflower sea star (*Pycnopodia helianthoides*) suffered the most catastrophic
¹⁵⁰ decline, losing an estimated 5.75 billion individuals and experiencing a 90.6% range-wide
¹⁵¹ population reduction based on 61,043 surveys across 31 datasets [19, 24]. Along the outer
¹⁵² coast from Washington to Baja California, declines exceeded 97%, with many regions
¹⁵³ recording zero individuals in subsequent surveys [19, 22]. The species was assessed as
¹⁵⁴ Critically Endangered by the IUCN in 2021 [19] and is under consideration for listing as
¹⁵⁵ Threatened under the U.S. Endangered Species Act [39].

¹⁵⁶ As a large-bodied, mobile, generalist predator capable of consuming sea urchins at
¹⁵⁷ rates sufficient to structure entire subtidal communities, *Pycnopodia helianthoides* func-
¹⁵⁸ tions as a keystone species in northeastern Pacific kelp forest ecosystems [6, 15, 44].
¹⁵⁹ Its precipitous decline has been linked to cascading trophic effects, including sea urchin
¹⁶⁰ population explosions and extensive kelp forest deforestation, with northern California
¹⁶¹ losing 96% of its kelp canopy since the 2014 marine heatwave [45, 51]. The loss of this
¹⁶² apex predator thus represents not only a conservation crisis for a single species but a
¹⁶³ destabilization of an entire marine ecosystem [22, 36].

¹⁶⁴ **1.2 Etiology: A Decade-Long Mystery Resolved**

¹⁶⁵ For over a decade following the initial outbreak, the causative agent of SSWD remained
¹⁶⁶ contested. An early hypothesis implicating sea star associated densovirus (SSaDV; Hew-
¹⁶⁷ son et al. 29) was subsequently retracted after repeated failures to reproduce the original
¹⁶⁸ challenge experiments and the discovery that the virus is endemic in healthy echinoderm
¹⁶⁹ populations worldwide [30–32]. An alternative hypothesis invoking boundary layer oxygen
¹⁷⁰ depletion (BLODL) at the animal–water interface proposed that microbial respiration on
¹⁷¹ sea star surfaces draws down dissolved oxygen, leading to tissue hypoxia [2, 27]. While
¹⁷² this mechanism may contribute to disease susceptibility, it did not identify a specific
¹⁷³ pathogen.

¹⁷⁴ The breakthrough came with Prentice et al. [49], who fulfilled Koch’s postulates by
¹⁷⁵ demonstrating that *Vibrio pectenicida* strain FHCF-3, a Gram-negative marine bac-

terium, is a causative agent of SSWD in *Pycnopodia helianthoides*. Through seven controlled exposure experiments using captive-bred, quarantined sea stars, the authors showed that injection of cultured *V. pectenicida* FHCF-3 into the coelomic cavity reliably produced disease signs — arm twisting, lesion formation, autotomy, and death within approximately two weeks. Heat-treated and 0.22 µm filtered controls remained healthy, confirming a living bacterial agent. Critically, the pathogen was re-isolated from experimentally infected animals, completing Koch’s postulates. Earlier investigations had missed *V. pectenicida* because they sampled body wall tissue rather than coelomic fluid, where the bacterium resides.

However, the etiological picture is not entirely resolved. Hewson [28] demonstrated that *V. pectenicida* FHCF-3 was not consistently detected in non-*Pycnopodia helianthoides* species during the 2013–2014 mass mortality, suggesting it may be specific to *Pycnopodia helianthoides* or may function as an opportunistic pathogen rather than a universal SSWD agent across all affected asteroid taxa. The bacterium also exhibits explosive growth in the presence of decaying echinoderm tissue, raising questions about whether it acts primarily as a pathogen or a saprobe under different conditions [28]. Nonetheless, for *Pycnopodia helianthoides* — the focus of this study — the evidence for *V. pectenicida* as the primary causative agent is robust. The identification of a specific bacterial pathogen with known temperature-dependent growth dynamics [42] provides a mechanistic basis for modeling disease transmission and environmental forcing.

1.3 Conservation Urgency and Active Recovery Efforts

The failure of *Pycnopodia helianthoides* populations to recover naturally in the decade following the initial epizootic — contrasting with partial recovery observed in some co-occurring asteroid species [18] — has motivated intensive conservation action. The species’ long generation time (~30 years), broadcast spawning reproductive strategy, and vulnerability to Allee effects at low density [16, 40] compound the challenge of natural recovery. Historical precedent is sobering: the Caribbean long-spined sea urchin *Diadema antillarum*, which suffered a comparable 93–100% mass mortality in 1983–1984, achieved only ~12% recovery after three decades [37]. Another asteroid, *Heliaster kubiniji*, has never recovered from a 1975 mass mortality event in the Gulf of California [12].

In response, a coordinated multi-partner recovery effort has emerged. The Association of Zoos and Aquariums (AZA) Saving Animals From Extinction (SAFE) program maintains over 2,500 captive juveniles and 130+ reproductive adults across 17 AZA institutions [5]. The first experimental outplanting of captive-bred *Pycnopodia helianthoides* occurred in December 2025 in Monterey, California, with 47 of 48 juveniles surviving after four weeks [59]. A Roadmap to Recovery developed by over 30 leading experts defines regionally nested recovery objectives, from local demographic benchmarks to range-wide

213 genetic structure targets [24]. Cryopreservation of gametes has been demonstrated for a
214 congener and is under development for *Pycnopodia helianthoides* to enable assisted gene
215 flow from genetically diverse founders [21, 57]. In 2025, the California Ocean Protection
216 Council approved \$630,000 in funding for captive breeding, disease diagnostics, and ex-
217 perimental outplanting [7]. A reference genome has also been published [56], laying the
218 groundwork for genome-wide association studies (GWAS) to identify resistance loci.

219 These recovery efforts require quantitative predictions: How many captive-bred in-
220 dividuals should be released, where, and when? What are the genetic consequences of
221 releasing animals from a limited captive founder population? Can natural selection drive
222 resistance evolution fast enough to matter on conservation timescales? How do pathogen
223 evolution, environmental change, and spatial structure interact to shape recovery trajec-
224 tories? Answering these questions demands a modeling framework that integrates disease
225 dynamics with population genetics in an explicitly spatial context.

226 1.4 The Need for an Eco-Evolutionary Framework

227 Existing models of SSWD dynamics have focused on either epidemiological or ecological
228 aspects in isolation. Aalto et al. [1] coupled an SIR-type model with ocean circulation to
229 explain the rapid continental-scale spread of SSWD, finding that temperature-dependent
230 mortality best matched observed patterns. Tolimieri [60] conducted a population viability
231 analysis using stage-structured matrix models but did not incorporate disease dynamics or
232 host genetics. Arroyo-Esquivel et al. [4] recently modeled epidemiological consequences of
233 managed reintroduction following disease-driven host decline, but their framework lacks
234 genetic evolution. None of these approaches captures the interplay between disease-driven
235 selection, host genetic adaptation, and demographic recovery that is central to predicting
236 conservation outcomes.

237 The theoretical motivation for coupling these processes is compelling. Mass mortal-
238 ity events impose intense directional selection on host populations [54], and in *Pisaster*
239 *ochraceus* — a co-occurring sea star affected by SSWD — rapid allele frequency shifts
240 ($\Delta q \approx 0.08\text{--}0.15$ at outlier loci) were detected within a single generation of the epi-
241 zotic, with geographic consistency across sites indicating selection rather than drift [54].
242 However, in broadcast-spawning marine invertebrates, the genetic consequences of mass
243 mortality are filtered through sweepstakes reproductive success (SRS), whereby variance
244 in individual reproductive success is so large that effective population size (N_e) is orders
245 of magnitude smaller than census size ($N_e/N \sim 10^{-3}$; Árnason et al. 3, Hedgecock and
246 Pudovkin 25). SRS amplifies genetic drift on ecological timescales [61], can facilitate rapid
247 adaptation when coupled with bottlenecks [14], and generates chaotic genetic patchiness
248 that confounds simple predictions of evolutionary trajectories. Any model of evolutionary
249 rescue in *Pycnopodia helianthoides* must therefore account for this fundamental feature

250 of marine broadcast spawner genetics.

251 The closest methodological precedent is the eco-evolutionary individual-based model
252 (IBM) developed by Clement et al. [10] for coevolution between Tasmanian devils (*Sar-*
253 *cophilus harrisii*) and devil facial tumour disease (DFTD). That model coupled an SEI
254 epidemiological framework with polygenic quantitative genetics, parameterized from two
255 decades of field data and GWAS results, and found a high probability of host persistence
256 over 50 generations through coevolutionary dynamics. Our model extends this approach
257 to a marine system with fundamentally different reproductive biology — broadcast spawn-
258 ing with sweepstakes reproductive success, external fertilization subject to Allee effects,
259 and a pelagic larval phase mediating spatial connectivity — challenges that no existing
260 eco-evolutionary disease model has addressed.

261 1.5 Model Overview

262 We present SSWD-EvoEpi, an individual-based, spatially explicit, eco-evolutionary epi-
263 demiological model designed to simulate SSWD dynamics and evolutionary responses in
264 *Pycnopodia helianthoides* metapopulations across the northeastern Pacific. The model
265 tracks individual sea stars as agents within a network of habitat nodes connected by larval
266 dispersal and pathogen transport. Each agent carries a diploid genotype across 51 loci
267 governing three fitness-related traits: resistance (r_i , 17 loci; immune exclusion reducing
268 infection probability), tolerance (t_i , 17 loci; damage limitation extending survival dur-
269 ing late-stage infection), and recovery (c_i , 17 loci; pathogen clearance enabling transition
270 from infected to recovered states). Per-locus allele frequencies are drawn from a Beta(2,8)
271 distribution, reflecting polygenic architecture with most loci at low frequency [34].

272 Disease dynamics follow an SEIR-type compartmental structure with exposed (E),
273 early infected (I_1), and late infected (I_2) stages, coupled with an environmental pathogen
274 reservoir (P) whose dynamics are temperature-dependent [17, 42]. Pathogen evolution
275 is modeled through a heritable virulence phenotype that evolves along a mechanistic
276 tradeoff curve linking shedding rate to host survival duration. Reproduction incorpo-
277 rates sweepstakes reproductive success via a heavy-tailed offspring distribution producing
278 N_e/N ratios consistent with empirical estimates for marine broadcast spawners [25], with
279 sex-asymmetric spawning induction and post-spawning immunosuppression derived from
280 species-specific observations. Spatial connectivity is implemented through distinct larval
281 exchange and pathogen dispersal matrices computed from overwater distances across the
282 model domain.

283 The model is implemented in Python with NumPy-vectorized agent operations, achiev-
284 ing sufficient performance for large-scale sensitivity analysis and calibration (75,000 agents
285 across 150 nodes in ~ 72 s). Four rounds of sensitivity analysis using Morris screening and
286 Sobol variance decomposition across up to 47 parameters have identified the key drivers of

287 model behavior, revealing strong nonlinear interactions and highlighting priority targets
288 for empirical calibration.

289 1.6 Paper Outline

290 The remainder of this paper is organized as follows. Section 2 describes the overall model
291 architecture, agent representation, and simulation flow. Sections 3–6 detail the disease,
292 genetics, population dynamics, and spatial modules, respectively. Section 7 presents four
293 rounds of global sensitivity analysis, identifying the parameters with greatest influence
294 on epidemiological, demographic, and evolutionary outcomes. Section 8 describes model
295 validation against available empirical data. Section 9 synthesizes findings, discusses lim-
296 itations, and outlines the path toward calibrated conservation scenario evaluation. Pa-
297 rameter tables and supplementary analyses are provided in Appendix A.

298 2 Model Architecture

299 SSWD-EvoEpi is an individual-based model (IBM) that couples epidemiological, demo-
300 graphic, genetic, and spatial dynamics to simulate the eco-evolutionary consequences of
301 sea star wasting disease in *Pycnopodia helianthoides*. Each agent represents a single sea
302 star tracked through its complete life history, carrying a diploid genotype at 51 loci that
303 determines three quantitative defense traits against *Vibrio pectenicida*. We chose an
304 individual-based approach over compartmental (ODE/PDE) models because SSWD dy-
305 namics depend critically on individual-level heterogeneity in genetic resistance, body size,
306 spatial position, and disease stage—features that compartmental models cannot represent
307 without substantial loss of biological realism [11, 20].

308 2.1 Agent Representation

309 Each individual is represented as a record in a NumPy structured array (`AGENT_DTYPE`)
310 comprising approximately 59 bytes per agent. Table 1 summarizes the principal state
311 variables grouped by functional module.

Table 1: Agent state variables in SSWD-EvoEpi.

Module	Field	Description
Spatial	x, y	Position within node habitat (m)
	heading	Movement heading (rad)
	speed	Instantaneous speed (m min^{-1})
	node_id	Home node index
Life history	size	Arm-tip diameter (mm)
	age	Age (years, fractional)
	stage	Life stage (0–4; Table 2)
	sex	Sex (0 = female, 1 = male)
Disease	disease_state	Compartment (S/E/I ₁ /I ₂ /D/R)
	disease_timer	Days remaining in current disease stage
Genetics	resistance	Resistance score $r_i \in [0, 1]$
	tolerance	Tolerance score $t_i \in [0, 1]$
	recovery_ability	Recovery/clearance score $c_i \in [0, 1]$
Spawning	has_spawned	Bout count this season
	immunosuppression_timer	Post-spawning immunosuppression (days)
Administrative	alive	Active flag
	origin	Wild / captive-bred / AGF / wild-source
	pathogen_virulence	Virulence of infecting strain v_i

312 Genotypes are stored in a separate array of shape $(N_{\text{max}}, 51, 2)$ with `int8` entries,
 313 where axis 1 indexes loci and axis 2 indexes the two allele copies (diploid). This separation
 314 from the agent record improves cache performance during non-genetic operations (disease
 315 transmission, movement), which need not touch the genotype array.

Table 2: Life stages and size thresholds for *Pycnopodia helianthoides*.

Index	Stage	Size threshold (mm)	Reproductive
0	Egg/Larva	—	No
1	Settler	Settlement	No
2	Juvenile	≥ 10	No
3	Subadult	≥ 150	No
4	Adult	≥ 400	Yes

316 **2.2 Node Structure**

317 The spatial domain is represented as a metapopulation network of K discrete habitat
318 nodes. Each node encapsulates:

- 319 • A population of agents (structured array + genotype array), initialized at local
320 carrying capacity;
- 321 • Environmental state: sea surface temperature $T(t)$ (sinusoidal annual cycle with
322 warming trend), salinity S , and tidal flushing rate ϕ_k ;
- 323 • A local Vibrio concentration $P_k(t)$ (bacteria mL $^{-1}$);
- 324 • Node metadata: latitude, habitat area, fjord classification.

325 Inter-node coupling occurs through two connectivity matrices:

- 326 1. **Pathogen dispersal matrix D:** governs daily exchange of waterborne *Vibrio*
327 *pectenicida* between nodes, parameterized with an exponential distance kernel (scale
328 $D_P = 15$ km);
- 329 2. **Larval connectivity matrix C:** governs annual dispersal of competent larvae
330 among nodes, parameterized with a broader kernel (scale $D_L = 400$ km) reflecting
331 the extended pelagic larval duration of *Pycnopodia helianthoides*.

332 **2.3 Simulation Loop**

333 The simulation advances in daily timesteps ($\Delta t = 1$ day) nested within an annual cycle.
334 At each daily step, the following operations are executed in sequence at every node
335 (Figure ??):

- 336 1. **Environment update.** Compute $T_k(t)$ from a sinusoidal annual SST function
337 with linear warming trend; update flushing rate ϕ_k (seasonally modulated for fjord
338 nodes); salinity is constant per node.
- 339 2. **Movement.** Agents execute a correlated random walk (CRW) with 24 hourly
340 substeps per day. Movement speed is modulated by disease state ($\times 0.5$ for I₁, $\times 0.1$
341 for I₂, $\times 0$ for D). Elastic boundary reflection constrains agents within the habitat.
- 342 3. **Disease dynamics.** Vibrio concentration is updated via an Euler step of the
343 pathogen ODE. Susceptible agents are exposed to a force of infection that depends
344 on local pathogen density, individual resistance, salinity, and body size. Infected
345 agents progress through the SEIPD+R compartments with Erlang-distributed stage
346 durations (Section 3).

- 347 4. **Pathogen dispersal.** Vibrio is exchanged between neighboring nodes via the **D**
 348 matrix, representing waterborne transport.
- 349 5. **Settlement.** Larval cohorts whose pelagic larval duration (PLD) has elapsed are
 350 settled into the local population via Beverton–Holt density-dependent recruitment,
 351 modulated by an adult-presence settlement cue (Allee effect).
- 352 6. **Spawning.** During the spawning season (November–July), reproductively mature
 353 adults spawn stochastically with daily probability modulated by a seasonal Gaus-
 354 sian envelope centered on the peak spawning day. Female and male multi-bout
 355 spawning, sex-asymmetric cascade induction, and post-spawning immunosuppres-
 356 sion are modeled explicitly.
- 357 7. **Daily demographics.** Natural mortality is applied as a daily probability con-
 358 verted from stage-specific annual survival rates:

$$p_{\text{death,daily}} = 1 - S_{\text{annual}}^{1/365}, \quad (1)$$

359 with a senescence overlay for individuals exceeding the senescence age ($\tau_{\text{sen}} = 50 \text{ yr}$).
 360 Growth follows the von Bertalanffy differential form with daily-scaled stochastic
 361 noise; stage transitions are one-directional based on size thresholds (Table 2).

362 At the end of each simulated year, an annual step performs:

- 363 1. **Larval dispersal** via the connectivity matrix **C**: unsettled cohorts from all nodes
 364 are pooled, redistributed probabilistically among destination nodes, and settled at
 365 receiving nodes or retained in a pending queue for next-year daily settlement.
- 366 2. **Disease introduction** (at the designated epidemic year): a fixed number of agents
 367 per node are seeded in the Exposed (E) compartment.
- 368 3. **Genetic recording**: per-node allele frequencies, additive genetic variance V_A , and
 369 trait means are logged annually. Pre- and post-epidemic allele frequency snapshots
 370 are captured for calibration against genomic data.

371 2.4 Design Rationale

372 Several design choices distinguish SSWD-EvoEpi from previous SSWD models:

373 **Individual-based representation.** SSWD mortality is strongly size-dependent [OR
 374 = 1.23 per 10 mm; 13], genetically mediated [55], and spatially heterogeneous. A compart-
 375 mental SIR/SEIR model would require aggregating these axes of variation into homoge-
 376 neous classes, losing the emergent eco-evolutionary dynamics that arise from individual

377 heterogeneity in resistance, tolerance, and recovery. Following Clement et al. [9], who
378 demonstrated that individual-based eco-evolutionary models are essential for predicting
379 host-pathogen coevolution in Tasmanian devil facial tumor disease, we track each indi-
380 vidual’s genotype, phenotype, and infection history explicitly.

381 **Continuous daily demographics.** Rather than applying mortality, growth, and re-
382 production as annual pulses, SSWD-EvoEpi evaluates natural mortality and growth daily
383 (Eq. 1), with spawning resolved to individual daily events across a multi-month season.
384 This avoids artificial synchronization artifacts and allows disease-demography interac-
385 tions (e.g., post-spawning immunosuppression) to operate on their natural timescales.

386 **Separated genotype storage.** The 51-locus diploid genotype array (102 bytes per
387 agent) is stored separately from the agent state record. This ensures that the most
388 frequently accessed fields during daily disease and movement updates (position, disease
389 state, size) occupy contiguous memory, improving CPU cache performance by a factor of
390 $\sim 2\text{--}3 \times$ in profiled benchmarks.

391 **Three-trait genetic architecture.** The 51 loci are partitioned into three indepen-
392 dently segregating trait blocks of 17 loci each, controlling resistance (immune exclusion),
393 tolerance (damage limitation), and recovery (pathogen clearance). This architecture
394 captures the empirical observation that host defense against infectious disease operates
395 through mechanistically distinct pathways that can evolve semi-independently [50].

396 3 Disease Module

397 The disease module implements a stochastic, environmentally driven SEIPD+R (Susceptible–
398 Exposed–Infectious₁–Infectious₂–Dead, plus Recovered) compartmental framework oper-
399 ating at the individual level. Each agent carries its own disease state, countdown timer,
400 genetic defense traits (r_i, t_i, c_i), and (when pathogen evolution is enabled) the virulence
401 phenotype v_i of its infecting strain. Disease dynamics are resolved daily at each spatial
402 node, coupled to the environmental forcing module for temperature-dependent rates and
403 to the genetics module for individual susceptibility.

404 3.1 Compartmental Structure

405 The disease pathway consists of five compartments plus a recovery state (Figure ??):

- 406 • **S (Susceptible):** Healthy, at risk of infection.
- 407 • **E (Exposed):** Latently infected; not yet shedding pathogen. Duration is Erlang-
408 distributed with shape $k_E = 3$.

- **I₁ (Early infectious):** Pre-symptomatic shedding at rate $\sigma_1(T)$. Duration is Erlang-distributed with shape $k_{I_1} = 2$. Agents with high clearance ability ($c_i > 0.5$) may recover early.
- **I₂ (Late infectious):** Symptomatic wasting with high shedding rate $\sigma_2(T)$. Duration is Erlang-distributed with shape $k_{I_2} = 2$. Agents may recover with probability $p_{\text{rec}} = \rho_{\text{rec}} \times c_i$ per day.
- **D (Dead from disease):** Carcass continues to shed pathogen saprophytically for a 3-day window at rate σ_D .
- **R (Recovered):** Immune; functionally equivalent to S for demographics but not susceptible to reinfection.

3.1.1 Erlang-Distributed Stage Durations

Durations in compartments E, I₁, and I₂ are drawn from Erlang distributions rather than geometric (exponential) distributions. The Erlang distribution with shape parameter k and rate parameter $k\mu$ has mean $1/\mu$ and coefficient of variation $CV = 1/\sqrt{k}$, producing more realistic, peaked duration distributions compared to the memoryless exponential [63]. For each individual entering a compartment, a duration is sampled as:

$$\tau \sim \text{Erlang}(k, k\mu(T)), \quad \text{rounded to } \max(1, \text{round}(\tau)) \text{ days}, \quad (2)$$

where $\mu(T)$ is the temperature-dependent transition rate at the current SST (Section 3.3.2). The shape parameters are:

$$k_E = 3 \quad (CV = 0.58), \quad k_{I_1} = 2 \quad (CV = 0.71), \quad k_{I_2} = 2 \quad (CV = 0.71). \quad (3)$$

Timers count down by one each day; when the timer reaches zero, the agent transitions to the next compartment.

3.2 Force of Infection

The per-individual instantaneous hazard rate of infection is:

$$\lambda_i = a_{\text{exp}} \underbrace{\frac{P_k}{K_{1/2} + P_k}}_{\text{dose-response}} \underbrace{(1 - r_i)}_{\text{resistance}} \underbrace{S_{\text{sal}}}_{\text{salinity}} \underbrace{f_{\text{size}}(L_i)}_{\text{size}}, \quad (4)$$

where:

- $a_{\text{exp}} = 0.75 \text{ d}^{-1}$ is the baseline exposure rate;

- 433 • P_k is the local Vibrio concentration (bacteria mL⁻¹) at node k ;
- 434 • $K_{1/2} = 87,000$ bacteria mL⁻¹ is the half-infective dose (Michaelis–Menten dose–
435 response);
- 436 • $r_i \in [0, 1]$ is the individual’s resistance score (immune exclusion; Section 4);
- 437 • S_{sal} is the salinity modifier (Section 3.2.2);
- 438 • $f_{\text{size}}(L_i)$ is the size-dependent susceptibility modifier (Section 3.2.3).

439 The discrete daily probability of infection is:

$$p_{\text{inf}} = 1 - \exp(-\lambda_i \Delta t), \quad \Delta t = 1 \text{ day.} \quad (5)$$

440 3.2.1 Dose–Response Function

441 Pathogen exposure follows a Michaelis–Menten (saturating) dose–response:

$$D(P_k) = \frac{P_k}{K_{1/2} + P_k}. \quad (6)$$

442 At low concentrations ($P_k \ll K_{1/2}$), infection probability scales linearly with pathogen
443 density; at high concentrations ($P_k \gg K_{1/2}$), it saturates at $D \rightarrow 1$, reflecting physiolog-
444 ical limits on pathogen uptake.

445 3.2.2 Salinity Modifier

446 Vibrio viability is suppressed at low salinities, providing a mechanistic basis for the
447 reduced SSWD prevalence observed in fjord systems:

$$S_{\text{sal}} = \begin{cases} 0 & \text{if } S \leq S_{\text{min}} = 10 \text{ psu,} \\ \left(\frac{S - S_{\text{min}}}{S_{\text{full}} - S_{\text{min}}} \right)^{\eta} & \text{if } S_{\text{min}} < S < S_{\text{full}}, \\ 1 & \text{if } S \geq S_{\text{full}} = 28 \text{ psu,} \end{cases} \quad (7)$$

448 where $\eta = 2$ produces a convex response (low salinity is strongly protective).

449 3.2.3 Size-Dependent Susceptibility

450 Larger *Pycnopodia helianthoides* are more susceptible to SSWD, consistent with the em-
451 pirical finding of Eisenlord et al. [13] (odds ratio 1.23 per 10 mm increase in radius). The
452 size modifier is:

$$f_{\text{size}}(L_i) = \exp\left(\beta_L \frac{L_i - \bar{L}}{\sigma_L}\right), \quad (8)$$

453 where $\beta_L = 0.021 \text{ mm}^{-1}$ ($= \ln 1.23/10$), $\bar{L} = 300 \text{ mm}$ is the reference size, and $\sigma_L =$
 454 100 mm normalizes the deviation. An individual of diameter $L_i = 500 \text{ mm}$ has $\sim 1.5 \times$ the
 455 infection hazard of a 300 mm individual.

456 3.2.4 Post-Spawning Immunosuppression

457 Spawning imposes a transient immune cost. Following each spawning event, an individ-
 458 ual enters a 28-day immunosuppression window during which its effective resistance is
 459 reduced:

$$r_{i,\text{eff}} = \frac{r_i}{\psi_{\text{spawn}}}, \quad \psi_{\text{spawn}} = 2.0, \quad (9)$$

460 clamped to $[0, 1]$. This halves effective resistance during the immunosuppressed period,
 461 creating an evolutionary coupling between reproductive investment and disease vulnera-
 462 bility.

463 3.3 Disease Progression and Recovery

464 Disease progression rates are temperature-dependent via an Arrhenius function (Sec-
 465 tion 3.3.2). At each daily step, disease timers are decremented; when a timer reaches
 466 zero, the agent transitions to the next state. Recovery can occur before timer expiry.

467 3.3.1 Transition Rates

468 The base progression rates at reference temperature $T_{\text{ref}} = 20^\circ\text{C}$ are:

$$\mu_{E \rightarrow I_1} = 0.57 \text{ d}^{-1} \quad (E_a/R = 4,000 \text{ K}), \quad (10)$$

$$\mu_{I_1 \rightarrow I_2} = 0.40 \text{ d}^{-1} \quad (E_a/R = 5,000 \text{ K}), \quad (11)$$

$$\mu_{I_2 \rightarrow D} = 0.173 \text{ d}^{-1} \quad (E_a/R = 2,000 \text{ K}). \quad (12)$$

469 The activation energy for $I_2 \rightarrow D$ is notably lower ($E_a/R = 2,000 \text{ K}$ vs. $5,000\text{--}6,000 \text{ K}$ for
 470 other transitions), reflecting evidence that terminal wasting is less temperature-sensitive
 471 than earlier disease stages (Errata E1).

472 3.3.2 Temperature Scaling (Arrhenius)

473 All temperature-dependent rates are scaled via the Arrhenius equation:

$$k(T) = k_{\text{ref}} \exp \left[\frac{E_a}{R} \left(\frac{1}{T_{\text{ref}}} - \frac{1}{T} \right) \right], \quad (13)$$

474 where $T_{\text{ref}} = 293.15 \text{ K}$ (20°C) is the reference temperature corresponding to the *Vibrio*
 475 *pectenicida* thermal optimum [35], and E_a/R is the activation energy divided by the
 476 gas constant. The Arrhenius formulation ensures that colder temperatures slow disease

⁴⁷⁷ progression (longer E, I₁, I₂ durations) and reduce shedding rates, consistent with the
⁴⁷⁸ observed latitudinal gradient in SSWD severity.

⁴⁷⁹ 3.3.3 Tolerance: Extending I₂ Duration

⁴⁸⁰ The tolerance trait t_i operates as a damage-limitation mechanism that reduces the effec-
⁴⁸¹ tive I₂ → D mortality rate, extending survival time while infected:

$$\mu_{I_2 \rightarrow D, \text{eff}} = \mu_{I_2 \rightarrow D}(T) \times (1 - t_i \tau_{\max}), \quad \text{floored at } 0.05 \times \mu_{I_2 \rightarrow D}(T), \quad (14)$$

⁴⁸² where $\tau_{\max} = 0.85$ is the maximum mortality reduction at $t_i = 1$. The floor prevents
⁴⁸³ biologically implausible indefinite survival. The effective rate is used when sampling the
⁴⁸⁴ I₂ timer (Eq. 2), so tolerant individuals spend longer in I₂— which may prolong both
⁴⁸⁵ recovery opportunity and pathogen shedding.

⁴⁸⁶ 3.3.4 Recovery

⁴⁸⁷ Recovery from infection proceeds via the clearance trait c_i , which represents the host's
⁴⁸⁸ capacity for pathogen elimination.

⁴⁸⁹ **Recovery from I₂.** Each day, an I₂ individual has probability:

$$p_{\text{rec}, I_2} = \rho_{\text{rec}} \times c_i, \quad \rho_{\text{rec}} = 0.05 \text{ d}^{-1}, \quad (15)$$

⁴⁹⁰ of transitioning to the R compartment. At $c_i = 0$ (no clearance ability), recovery is
⁴⁹¹ impossible; at $c_i = 1$, the daily recovery probability is 5%.

⁴⁹² **Early recovery from I₁.** Individuals with exceptionally high clearance ability ($c_i >$
⁴⁹³ 0.5) can recover during the pre-symptomatic stage:

$$p_{\text{rec}, I_1} = \begin{cases} 0 & \text{if } c_i \leq 0.5, \\ \rho_{\text{rec}} \times 2(c_i - 0.5) & \text{if } c_i > 0.5. \end{cases} \quad (16)$$

⁴⁹⁴ At $c_i = 1.0$, the early recovery probability equals ρ_{rec} , identical to I₂ recovery at maximum
⁴⁹⁵ clearance. The threshold at $c_i = 0.5$ ensures that only rare, high-clearance individuals
⁴⁹⁶ can clear infection before progressing to the symptomatic stage.

497 **3.4 Vibrio Dynamics**

498 The concentration of waterborne *Vibrio pectenicida* at node k evolves according to:

$$\frac{dP_k}{dt} = \underbrace{\sigma_1(T) n_{I_1} + \sigma_2(T) n_{I_2} + \sigma_D n_{D,\text{fresh}}}_{\text{shedding}} - \underbrace{\xi(T) P_k}_{\text{decay}} - \underbrace{\phi_k P_k}_{\text{flushing}} + \underbrace{P_{\text{env}}(T, S)}_{\text{reservoir}} + \underbrace{\sum_j d_{jk} P_j}_{\text{dispersal}}, \quad (17)$$

499 integrated via forward Euler with $\Delta t = 1$ day, subject to $P_k \geq 0$.

500 **3.4.1 Shedding**

501 Pathogen shedding from live infectious hosts is temperature-dependent:

$$\sigma_1(T) = 5.0 \times \text{Arr}(T) \quad (\text{I}_1: \text{pre-symptomatic}), \quad (18)$$

$$\sigma_2(T) = 50.0 \times \text{Arr}(T) \quad (\text{I}_2: \text{symptomatic}), \quad (19)$$

502 where $\text{Arr}(T)$ denotes the Arrhenius factor (Eq. 13) with $E_a/R = 5,000$ K. The 10-
503 fold difference between early and late shedding reflects the dramatic increase in tissue
504 degradation and pathogen release during the wasting phase. Rates are given in bacte-
505 ria $\text{mL}^{-1} \text{d}^{-1}$ host $^{-1}$ and represent field-effective values (Errata E2).

506 **3.4.2 Carcass Shedding**

507 Dead individuals (D compartment) continue to shed pathogen saprophytically for a 3-day
508 window at a constant rate $\sigma_D = 15$ bacteria $\text{mL}^{-1} \text{d}^{-1}$ carcass $^{-1}$ (field-effective; Code Err-
509 ata CE-6). A ring buffer of daily disease death counts over the most recent 3 days tracks
510 the number of “fresh” carcasses contributing to shedding:

$$n_{D,\text{fresh}}(t) = \sum_{\tau=0}^2 \text{deaths}(t - \tau). \quad (20)$$

511 **3.4.3 Vibrio Decay**

512 *Vibrio pectenicida* survives longer in warmer water. The natural decay rate $\xi(T)$ is
513 interpolated log-linearly between empirical estimates:

$$\xi(T) = \begin{cases} 1.0 \text{ d}^{-1} & T \leq 10^\circ\text{C} \text{ (half-life } \approx 0.7 \text{ d}), \\ 0.33 \text{ d}^{-1} & T \geq 20^\circ\text{C} \text{ (half-life } \approx 2.1 \text{ d}), \\ \exp[(1-f) \ln \xi_{10} + f \ln \xi_{20}] & \text{otherwise}, \end{cases} \quad (21)$$

514 where $f = (T - 10)/10$ and values are clamped outside the 10–20 °C range. This counter-
515 intuitive pattern (faster decay at cold temperatures) reflects the environmental Vibrio

516 literature [41].

517 3.4.4 Environmental Reservoir

518 In the ubiquitous scenario (default), *Vibrio pectenicida* is assumed to persist in the sed-
 519 iment as viable-but-non-culturable (VBNC) cells that resuscitate when SST exceeds a
 520 threshold. The background input rate is:

$$P_{\text{env}}(T, S) = P_{\text{env,max}} \underbrace{\frac{1}{1 + e^{-\kappa_{\text{VBNC}}(T - T_{\text{VBNC}})}}}_{\text{VBNC sigmoid}} \underbrace{g_{\text{peak}}(T)}_{\text{thermal performance}} \underbrace{S_{\text{sal}}}_{\text{salinity}}, \quad (22)$$

521 where:

- 522 • $P_{\text{env,max}} = 500 \text{ bacteria mL}^{-1} \text{ d}^{-1}$ is the maximum input rate;
- 523 • $\kappa_{\text{VBNC}} = 1.0 \text{ }^{\circ}\text{C}^{-1}$ controls the steepness of VBNC resuscitation;
- 524 • $T_{\text{VBNC}} = 12 \text{ }^{\circ}\text{C}$ is the midpoint temperature;
- 525 • $g_{\text{peak}}(T)$ is a thermal performance curve with Arrhenius increase below $T_{\text{opt}} = 20 \text{ }^{\circ}\text{C}$
 526 and quadratic decline above, reaching zero at $T_{\text{max}} = 30 \text{ }^{\circ}\text{C}$.

527 In the invasion scenario, $P_{\text{env}} = 0$ everywhere until the pathogen is explicitly intro-
 528 duced.

529 3.5 Pathogen Evolution

530 When pathogen evolution is enabled, each infectious agent carries a continuous virulence
 531 phenotype v_i that modulates disease rates via mechanistic tradeoff functions.

532 3.5.1 Virulence–Tradeoff Curves

533 More virulent strains kill faster, shed more, and progress more rapidly, but also remove
 534 themselves from the host population sooner:

$$\sigma_{1,v}(T) = \sigma_1(T) \times \exp(\alpha_{\text{shed}} \gamma_{\text{early}} (v - v^*)), \quad (23)$$

$$\sigma_{2,v}(T) = \sigma_2(T) \times \exp(\alpha_{\text{shed}} (v - v^*)), \quad (24)$$

$$\mu_{I_1 \rightarrow I_2, v}(T) = \mu_{I_1 \rightarrow I_2}(T) \times \exp(\alpha_{\text{prog}} (v - v^*)), \quad (25)$$

$$\mu_{I_2 \rightarrow D, v}(T) = \mu_{I_2 \rightarrow D}(T) \times \exp(\alpha_{\text{kill}} (v - v^*)), \quad (26)$$

535 where $v^* = 0.5$ is the ancestral virulence (identity point), $\alpha_{\text{shed}} = 1.5$, $\alpha_{\text{prog}} = 1.0$,
 536 $\alpha_{\text{kill}} = 2.0$, and $\gamma_{\text{early}} = 0.3$ attenuates the shedding effect in the pre-symptomatic stage.

537 **3.5.2 Transmission and Mutation**

538 When a new infection occurs, the infecting strain is inherited either from a shedding
 539 individual (weighted by shedding rate) or from the environmental reservoir (with virulence
 540 $v_{\text{env}} = 0.5$). The probability of inheriting from a shedder is proportional to the total host-
 541 derived shedding relative to total pathogen input:

$$P(\text{from shedder}) = \frac{\sum_j \sigma_j(v_j, T)}{\sum_j \sigma_j(v_j, T) + P_{\text{env}}(T, S)}. \quad (27)$$

542 The inherited virulence is then subject to mutation:

$$v_{\text{new}} = \text{clip}(v_{\text{parent}} + \mathcal{N}(0, \sigma_{v,\text{mut}}^2), v_{\text{min}}, v_{\text{max}}), \quad (28)$$

543 with $\sigma_{v,\text{mut}} = 0.02$, $v_{\text{min}} = 0$, $v_{\text{max}} = 1$.

544 **3.6 Basic Reproduction Number**

545 The basic reproduction number provides a summary measure of epidemic potential at a
 546 node:

$$R_0 = \frac{a_{\text{exp}} S_0 (1 - \bar{r}) S_{\text{sal}}}{K_{1/2} (\xi(T) + \phi_k)} \left[\frac{\sigma_1(T)}{\mu_{I_1 \rightarrow I_2}(T)} + \frac{\sigma_2(T)}{\mu_{I_2 \rightarrow D,\text{eff}}(T) + \rho_{\text{rec}} \bar{c}} + \sigma_D \tau_D \right], \quad (29)$$

547 where S_0 is the number of susceptibles, \bar{r} and \bar{c} are population-mean resistance and
 548 recovery scores, $\mu_{I_2 \rightarrow D,\text{eff}}$ incorporates population-mean tolerance (Eq. 14), $\rho_{\text{rec}} \bar{c}$ adds the
 549 recovery exit rate from I_2 , and $\tau_D = 3$ days is the carcass shedding duration. The three
 550 bracketed terms represent the pathogen contribution from each infectious compartment
 551 (I_1 , I_2 , and D carcasses, respectively).

552 **3.7 Daily Update Sequence**

553 Within each daily timestep, the disease module executes the following steps in order:

- 554 1. **Update Vibrio concentration** via Euler integration of Eq. 17, using current
 555 compartment counts and environmental conditions.
- 556 2. **Transmission ($S \rightarrow E$):** For each susceptible agent, compute the force of infection
 557 λ_i (Eq. 4), convert to daily probability (Eq. 5), and draw a Bernoulli infection event.
 558 Newly exposed agents receive an Erlang-sampled E-stage timer. When pathogen
 559 evolution is active, the infecting strain is inherited and mutated (Section 3.5.2).
- 560 3. **Disease progression:** Decrement all disease timers. For agents with expired
 561 timers: $E \rightarrow I_1$, $I_1 \rightarrow I_2$ (with tolerance-adjusted timer), $I_2 \rightarrow D$. For agents with

active timers: check recovery from I_2 (Eq. 15) and early recovery from I_1 (Eq. 16).

4. **Carcass tracking:** Record today’s disease deaths in the 3-day ring buffer for saprophytic shedding.

5. **Update diagnostics:** Recount compartments, update cumulative statistics (total infections, deaths, recoveries), track peak prevalence and peak Vibrio.

All operations are vectorized using NumPy batch sampling and array-level random draws for computational efficiency, achieving $O(N)$ scaling in population size.

4 Genetics Module

The genetics module tracks a diploid genotype at 51 biallelic loci for every individual, partitioned into three quantitative defense traits: *resistance*, *tolerance*, and *recovery*. Genotypes are transmitted via Mendelian inheritance with free recombination, mutated at a per-allele rate $\mu = 10^{-8}$ per generation [43], and subject to natural selection through the coupling of trait scores to disease dynamics (Section 3). The module additionally implements sweepstakes reproductive success (SRS) to capture the extreme reproductive variance characteristic of broadcast-spawning marine invertebrates [25].

4.1 Three-Trait Architecture

Each individual carries a (51×2) genotype array of `int8` alleles, where the 51 loci are partitioned into three contiguous blocks:

Table 3: Three-trait genetic architecture. The partition is configurable (constraint: $n_R + n_T + n_C = 51$); the default 17/17/17 split is used in all analyses reported here.

Trait	Symbol	Loci	Indices	Mechanistic role
Resistance	r_i	$n_R = 17$	0–16	Immune exclusion: reduces probability of $S \rightarrow E$ transition
Tolerance	t_i	$n_T = 17$	17–33	Damage limitation: extends I_2 survival via mortality rate reduction
Recovery	c_i	$n_C = 17$	34–50	Pathogen clearance: daily probability of $I_1/I_2 \rightarrow R$ transition

These three traits represent biologically distinct immune strategies with different epidemiological consequences [50]:

- **Resistance** (r_i) acts *before* infection via receptor polymorphisms, barrier defenses, and innate pathogen recognition. Resistant individuals reduce pathogen pressure on the population by preventing shedding entirely.

- **Tolerance** (t_i) acts *during* infection via tissue repair, anti-inflammatory regulation, and metabolic compensation. Tolerant hosts survive longer while infected but continue to shed pathogen—they are epidemiological “silent spreaders” that maintain transmission pressure while saving themselves.
- **Recovery** (c_i) acts *during late infection* via coelomocyte phagocytosis and immune effector mobilization. Recovering hosts actively clear the pathogen and transition to an immune state (R), removing a shedding host from the population.

The locus count of 51 is motivated by Schiebelhut et al. [54], who identified ~ 51 loci under selection in *Pisaster ochraceus* SSWD survivors. No genome-wide association study (GWAS) data currently distinguish resistance, tolerance, and recovery loci in *P. helianthoides*; the equal 17/17/17 partition is a simplifying assumption whose sensitivity is explored via the n_R parameter in the global sensitivity analysis (Section 7). A reference genome for *P. helianthoides* is now available [56], enabling future empirical partitioning.

Removal of EF1A overdominant locus. An earlier model version included a 52nd locus representing the EF1A elongation factor with overdominant fitness effects, based on Wares and Schiebelhut [62] who documented allele frequency shifts at this locus in *Pisaster ochraceus* following SSWD. We removed this locus because (1) the EF1A finding is specific to *Pisaster* with no evidence of overdominance in *P. helianthoides*, and (2) a single overdominant locus imposed a hard floor on heterozygosity loss that was biologically unjustified for our focal species.

4.2 Trait Score Computation

At each locus ℓ , an individual carries two alleles $g_{\ell,0}, g_{\ell,1} \in \{0, 1\}$, where 1 denotes the derived (protective) allele and 0 the ancestral allele. Each locus within a trait block has a fixed effect size $e_\ell > 0$, and an individual’s trait score is the effect-weighted mean allele dosage:

$$\theta_i = \sum_{\ell \in \mathcal{L}_\theta} e_\ell \frac{g_{\ell,0} + g_{\ell,1}}{2} \quad (30)$$

where \mathcal{L}_θ denotes the locus set for trait $\theta \in \{r, t, c\}$ and $\theta_i \in [0, \sum e_\ell]$. Effect sizes within each trait block are normalized so $\sum_{\ell \in \mathcal{L}_\theta} e_\ell = 1$, bounding all trait scores to $[0, 1]$.

4.2.1 Effect Size Distribution

Per-locus effect sizes are drawn from an exponential distribution $e_\ell \sim \text{Exp}(\lambda = 1)$, normalized to sum to 1.0 within each trait, and sorted in descending order. This produces a distribution where a few loci have large effects and the remainder have small effects,

616 consistent with empirical QTL architectures for disease resistance traits [38]. A fixed
 617 seed ensures identical effect sizes across simulation runs. Each trait block receives inde-
 618 pendently drawn effect sizes.

619 4.2.2 Coupling to Disease Dynamics

620 The three traits feed into the disease module (Section 3) as follows:

621 1. **Resistance** reduces the per-individual force of infection:

$$\lambda_i = a \cdot \frac{P}{K_{1/2} + P} \cdot (1 - r_i) \cdot S_{\text{sal}} \cdot f_L(L_i) \quad (31)$$

622 where a is the exposure rate, P the local *Vibrio pectenicida* concentration, $K_{1/2}$
 623 the half-infective dose, S_{sal} the salinity modifier, and $f_L(L_i)$ the size-dependent
 624 susceptibility factor.

625 2. **Tolerance** reduces the $I_2 \rightarrow D$ transition rate via a timer-scaling mechanism:

$$\mu_{I_2D,i}^{\text{eff}} = \mu_{I_2D}(T) \cdot (1 - t_i \cdot \tau_{\max}) \quad (32)$$

626 where $\tau_{\max} = 0.85$ is the maximum mortality reduction achievable at $t_i = 1$. A
 627 floor of 5% of the baseline rate prevents complete elimination of disease mortality.
 628 Tolerant individuals survive longer while infected but continue shedding, creating
 629 a selective conflict between individual and population-level fitness.

630 3. **Recovery** determines the daily clearance probability:

$$p_{\text{rec},i} = \rho_{\text{rec}} \times c_i \quad (33)$$

631 where $\rho_{\text{rec}} = 0.05 \text{ d}^{-1}$ is the base recovery rate. Recovery from I_1 requires $c_i > 0.5$
 632 (early clearance); recovery from I_2 has no threshold. Successful recovery transitions
 633 the agent to the R (recovered, immune) compartment.

634 4.3 Genotype Initialization

635 Initial allele frequencies are drawn independently for each locus from a Beta distribution:

$$q_\ell \sim \text{Beta}(a, b) \quad (\text{default } a = 2, b = 8) \quad (34)$$

636 producing a right-skewed frequency spectrum where most protective alleles are rare
 637 ($\mathbb{E}[q] = a/(a + b) = 0.2$), consistent with standing variation in immune genes main-
 638 tained by mutation-selection balance. The raw frequencies are then rescaled per-trait so
 639 that the expected population-mean trait score equals a configurable target:

Table 4: Default target population-mean trait scores at initialization.

Trait	Target mean	Rationale
Resistance (r_i)	0.15	Pre-epidemic standing variation
Tolerance (t_i)	0.10	Moderate damage limitation
Recovery (c_i)	0.02	Rare standing variation for clearance

640 Recovery is initialized with the lowest mean because active pathogen clearance is assumed
 641 to be the rarest phenotype prior to epidemic exposure. Per-locus frequencies are clipped
 642 to $[0.001, 0.5]$ to prevent fixation at initialization while ensuring the derived allele never
 643 begins at majority frequency. Genotypes are then sampled assuming Hardy–Weinberg
 644 equilibrium at each locus: each allele copy is independently drawn as a Bernoulli trial
 645 with probability q_ℓ .

646 4.4 Mendelian Inheritance and Mutation

647 At reproduction, each offspring inherits one randomly chosen allele from each parent at
 648 every locus (independent assortment, no linkage). The vectorized implementation draws
 649 allele choices for all $n_{\text{offspring}} \times 51 \times 2$ positions simultaneously, then indexes into parental
 650 genotype arrays.

651 Mutations are applied to offspring genotypes at rate $\mu = 10^{-8}$ per allele per genera-
 652 tion [43]. The total number of mutations per cohort is drawn from a Poisson distribution:
 653 $n_{\text{mut}} \sim \text{Pois}(\mu \times n_{\text{offspring}} \times 51 \times 2)$. Each mutation flips the allele at a randomly chosen
 654 position ($0 \rightarrow 1$ or $1 \rightarrow 0$), providing bidirectional mutational pressure. At the de-
 655 fault mutation rate, mutations are negligible within the 20–100 year simulation horizon
 656 (expected $\sim 10^{-6}$ mutations per offspring), and evolution proceeds primarily through
 657 selection on standing variation.

658 4.5 Sweepstakes Reproductive Success

659 Broadcast-spawning marine invertebrates exhibit sweepstakes reproductive success (SRS):
 660 a tiny fraction of adults contribute the majority of surviving offspring in any given cohort
 661 [25]. This phenomenon produces N_e/N ratios on the order of 10^{-3} in empirical obser-
 662 vations [3] and dramatically amplifies genetic drift while simultaneously accelerating the
 663 fixation of favorable alleles in post-epidemic populations [14].

664 SSWD-EvoEpi implements SRS via a Pareto-weighted reproductive lottery. Each
 665 spawning adult receives a random weight drawn from a Pareto distribution with shape
 666 parameter α_{SRS} (default 1.35):

$$w_i \sim \text{Pareto}(\alpha_{\text{SRS}}) + 1 \quad (35)$$

667 Female weights are additionally multiplied by size-dependent fecundity (Section 5.5),
 668 so larger females that win the sweepstakes lottery contribute disproportionately:

$$\tilde{w}_{i,\text{female}} = w_i \times \left(\frac{L_i}{L_{\text{ref}}} \right)^b \quad (36)$$

669 where $b = 2.5$ is the fecundity allometric exponent and $L_{\text{ref}} = 500$ mm. Male weights
 670 use the raw Pareto draw without fecundity modulation. Parents are then sampled with
 671 replacement from the normalized weight distributions, and offspring receive Mendelian-
 672 inherited genotypes.

673 The Pareto shape $\alpha_{\text{SRS}} = 1.35$ was chosen to produce N_e/N ratios consistent with
 674 empirical estimates of $\sim 10^{-3}$ in marine broadcast spawners [3, 25]. A small annual
 675 variation in α (drawn from $\mathcal{N}(\alpha_{\text{SRS}}, \sigma_\alpha^2)$ with $\sigma_\alpha = 0.10$) produces temporal fluctuation
 676 in the variance of reproductive success across cohorts.

677 **Effective population size.** N_e is computed from the realized offspring distribution
 678 using the standard formula [25]:

$$N_e = \frac{4N - 2}{V_k + 2} \quad (37)$$

679 where N is the number of spawning parents and V_k is the variance in offspring number.
 680 Sex-specific N_e values are computed for females and males separately, then combined via
 681 harmonic mean: $N_e = 4N_{e,f}N_{e,m}/(N_{e,f} + N_{e,m})$.

682 4.6 Genetic Diagnostics and Tracking

683 The model records a suite of genetic summary statistics at each node at annual intervals:

684 • **Per-trait means and variances:** \bar{r} , \bar{t} , \bar{c} and $\text{Var}(r)$, $\text{Var}(t)$, $\text{Var}(c)$.

685 • **Additive genetic variance (V_A) per trait:**

$$V_{A,\theta} = \sum_{\ell \in \mathcal{L}_\theta} 2 e_\ell^2 q_\ell (1 - q_\ell) \quad (38)$$

686 where q_ℓ is the derived allele frequency at locus ℓ . V_A determines the potential rate
 687 of evolutionary response to selection.

688 • **Heterozygosity:** Observed (H_o) and expected (H_e) heterozygosity averaged across
 689 all 51 loci.

690 • **F_{ST} :** Weir–Cockerham-style F_{ST} across nodes, computed as $F_{ST} = \text{Var}(\bar{q})/[\bar{q}(1 - \bar{q})]$
 691 averaged across polymorphic loci.

- 692 • **Pre- and post-epidemic allele frequency snapshots:** Full 51-locus allele fre-
693 quency vectors taken immediately before pathogen introduction and two years after
694 the epidemic onset, enabling direct measurement of allele frequency shifts (Δq) at-
695 tributable to selection.

696 **No cost of resistance.** A cost-of-resistance parameter (fecundity penalty for high r_i)
697 was considered but excluded following discussion with the senior author. No empirical
698 evidence supports a measurable fecundity cost for disease resistance alleles in *P. he-
699 lianthoides*, and including an unparameterized cost would introduce a free parameter
700 with no calibration target. Fecundity depends solely on body size (Section 5.5).

701 4.7 Genotype Bank (Tier 2 Nodes)

702 For Tier 2 spatial nodes that use simplified demographics rather than full agent tracking,
703 the genetics module maintains a *genotype bank* of $N_{\text{bank}} = 100$ representative diploid
704 genotypes with associated frequency weights. The bank is created by random sampling
705 from the alive population and preserves all three trait scores and allele frequencies. When
706 agents migrate from a Tier 2 to a Tier 1 node, genotypes are expanded from the bank
707 using SRS-weighted sampling (Pareto weights \times bank frequency weights) to reconstruct
708 individual-level genetic variation.

709 5 Population Dynamics

710 The population dynamics module governs the complete life history of *Pycnopodia he-
711 lianthoides*: growth, natural mortality, reproduction, larval dispersal, and settlement.
712 All demographic processes operate on a daily timestep, integrated within the master sim-
713 ulation loop described in Section 2. Disease-driven mortality is handled by the disease
714 module (Section 3); coupling occurs through shared access to the agent array.

715 5.1 Life Stages

716 Each individual progresses through five life stages defined by size thresholds (Table 5).
717 Stage transitions are unidirectional: agents can only advance, never regress.

Table 5: Life stages and transition thresholds for *P. helianthoides*.

Stage	Size range	Transition at	Duration
Egg/Larva	Planktonic	Settlement event	49–146 days PLD
Settler	0.5–10 mm	≥ 10 mm	~ 1 year
Juvenile	10–150 mm	≥ 150 mm	$\sim 1\text{--}5$ years
Subadult	150–400 mm	≥ 400 mm	$\sim 5\text{--}10$ years
Adult	>400 mm	—	10–50+ years

718 5.2 Growth

719 Individual growth follows the von Bertalanffy (VB) growth model in differential form,
720 resolved daily:

$$L(t + \Delta t) = L_\infty - (L_\infty - L(t)) \cdot \exp(-k_{\text{growth}} \cdot \Delta t) \quad (39)$$

721 where $L_\infty = 1000$ mm is the asymptotic arm-tip diameter, $k_{\text{growth}} = 0.08 \text{ yr}^{-1}$ is the
722 Brody growth coefficient, and $\Delta t = 1/365 \text{ yr}$ for the daily timestep. Individual growth
723 variation is introduced through a multiplicative log-normal noise term applied to the daily
724 increment:

$$\Delta L_i = (L_{\text{det}} - L_i) \cdot \exp(\varepsilon_i), \quad \varepsilon_i \sim \mathcal{N}\left(0, \frac{\sigma_g}{\sqrt{365}}\right) \quad (40)$$

725 where $\sigma_g = 2.0$ mm is the annual growth noise scale and the $\sqrt{365}$ scaling preserves the
726 annual CV when integrated over daily steps. Size is constrained to never decrease (no
727 shrinking). Stage transitions are evaluated after each growth step based on the thresholds
728 in Table 5.

729 Aging proceeds at $1/365$ years per day, producing fractional ages that drive size-at-age
730 trajectories and determine eligibility for senescence mortality.

731 5.3 Natural Mortality

732 Natural mortality is resolved daily using continuous hazard rates derived from stage-
733 specific annual survival probabilities. The daily death probability for individual i is:

$$p_{\text{death},i} = 1 - (1 - m_{\text{annual}}(s_i))^{1/365} \quad (41)$$

734 where $m_{\text{annual}}(s) = 1 - S_{\text{annual}}(s)$ is the annual mortality rate for stage s . The annual sur-
735 vival schedule (Table 6) produces a type III survivorship curve with high settler/juvenile
736 mortality and low adult mortality, consistent with demographic estimates for long-lived
737 asteroids.

Table 6: Stage-specific annual survival rates.

Stage	Annual survival (S)	Annual mortality
Settler	0.001	0.999
Juvenile	0.03	0.97
Subadult	0.90	0.10
Adult	0.95	0.05
Senescent	0.98	0.02 (base)

738 **Senescence.** Individuals exceeding the senescence age ($a_{\text{sen}} = 50$ yr) accumulate addi-
739 tional mortality linearly:

$$m_{\text{total}}(s_i, a_i) = m_{\text{annual}}(s_i) + m_{\text{sen}} \cdot \frac{a_i - a_{\text{sen}}}{20} \quad (42)$$

740 where $m_{\text{sen}} = 0.10$ and the divisor of 20 scales the senescence ramp such that a 70-year-old
741 individual experiences an additional 10% annual mortality.

742 Daily mortality is applied via a single vectorized random draw across all alive agents,
743 converting stage-dependent annual rates to daily hazard probabilities. This continuous
744 approach avoids the artificial synchronization artifacts of annual batch mortality and
745 permits realistic within-year population fluctuations.

746 5.4 Spawning System

747 SSWD-EvoEpi implements a biologically detailed spawning system reflecting the ex-
748 tended reproductive season and cascading spawning behavior observed in *P. helianthoides*.

749 5.4.1 Spawning Season and Phenology

750 The spawning season extends from day 305 (\approx November 1) through day 196 (\approx July 15)
751 of the following year, spanning approximately 270 days and wrapping across the calendar
752 year boundary. Spawning intensity follows a Normal envelope centered on a latitude-
753 adjusted peak:

$$P_{\text{season}}(d) = \exp\left(-\frac{(\Delta d)^2}{2 \sigma_{\text{peak}}^2}\right) \quad (43)$$

754 where Δd is the shortest circular distance between day d and the peak day (accounting
755 for year wrapping), and $\sigma_{\text{peak}} = 60$ days is the standard deviation of the seasonal peak.
756 The peak day-of-year is latitude-dependent:

$$d_{\text{peak}}(\phi) = d_{\text{peak,base}} + \lceil (\phi - 40^\circ\text{N}) \times 3 \text{ d}/^\circ \rceil \quad (44)$$

757 where $d_{\text{peak,base}} = 105$ (\approx April 15) is the reference peak at 40°N , and higher-latitude
758 populations spawn approximately 3 days later per degree northward.

759 **5.4.2 Spontaneous Spawning**

760 Each day during the spawning season, mature adults (≥ 400 mm, Susceptible or Recovered
761 disease state) are first evaluated for *readiness*, a stochastic physiological state modulated
762 by the seasonal envelope $P_{\text{season}}(d)$. Once ready, individuals attempt spontaneous spawning
763 with sex-specific daily probabilities:

$$p_{\text{spawn,female}} = 0.012 \quad (45)$$

$$p_{\text{spawn,male}} = 0.0125 \quad (46)$$

764 These rates were calibrated to produce $\geq 80\%$ female spawning participation per season
765 and a mean of ~ 2.2 male bouts per season, consistent with the observation that males
766 spawn more frequently than females in broadcast-spawning asteroids.

767 **Bout limits and refractory periods.** Females are limited to a maximum of 2 spawning
768 bouts per season; males are limited to 3 bouts. Males enter a brief refractory period
769 between bouts (default 0 days, configurable) during which they cannot spawn, reflecting
770 the physiological recovery time for spermatogenesis.

771 **5.4.3 Cascade Induction**

772 Spawning by one individual can trigger spawning in nearby conspecifics via waterborne
773 chemical cues (spawning-induced spawning), producing the synchronous mass spawning
774 events observed in broadcast spawners. Induction operates over a 3-day chemical cue
775 persistence window and is strongly sex-asymmetric:

$$\kappa_{\text{fm}} = 0.80 \quad (\text{female} \rightarrow \text{male induction}) \quad (47)$$

$$\kappa_{\text{mf}} = 0.60 \quad (\text{male} \rightarrow \text{female induction}) \quad (48)$$

776 where κ_{fm} is the probability that a ready male spawns when a female within the cas-
777 cade radius (200 m) has spawned within the cue window. The female-to-male asymmetry
778 reflects the stronger spawning trigger provided by egg-associated chemical signals. Readi-
779 ness induction also operates: individuals not yet physiologically ready can be driven to
780 readiness by nearby spawning activity, with a daily probability of 0.5 when within a 300 m
781 detection radius.

782 **5.4.4 Post-Spawning Immunosuppression**

783 Spawning imposes a 28-day immunosuppression period during which the individual's force
784 of infection is multiplied by a susceptibility factor of 2.0:

$$\lambda_i^{\text{eff}} = \lambda_i \times \begin{cases} \chi_{\text{immuno}} = 2.0 & \text{if immunosuppression timer} > 0 \\ 1.0 & \text{otherwise} \end{cases} \quad (49)$$

785 This reflects the metabolic cost of gamete production and the documented increase in
786 disease susceptibility following reproductive investment in marine invertebrates. The
787 immunosuppression timer is reset each time an individual spawns, so multiple spawning
788 bouts within a season extend the vulnerability window. Immunosuppression timers are
789 decremented daily regardless of spawning season status.

790 **5.5 Fecundity**

791 Female fecundity follows an allometric relationship with body size:

$$F_i = F_0 \cdot \left(\frac{L_i}{L_{\text{ref}}} \right)^b \quad (50)$$

792 where $F_0 = 10^7$ eggs is the reference fecundity at $L_{\text{ref}} = 500$ mm and $b = 2.5$ is the
793 allometric exponent. Only females at or above the minimum reproductive size $L_{\min} =$
794 400 mm produce eggs. No cost-of-resistance penalty is applied to fecundity (Section 4.6).

795 **5.6 Fertilization Kinetics and the Allee Effect**

796 Broadcast spawners face a fertilization Allee effect: at low population density, sperm lim-
797 itation reduces the fraction of eggs successfully fertilized [16, 40]. We model fertilization
798 success using a mean-field approximation of the Lundquist and Botsford [40] broadcast
799 fertilization model:

$$\mathcal{F}(\rho_m) = 1 - \exp(-\gamma_{\text{fert}} \cdot \rho_{m,\text{eff}}) \quad (51)$$

800 where $\gamma_{\text{fert}} = 4.5 \text{ m}^2$ is the sperm contact parameter and $\rho_{m,\text{eff}}$ is the effective male density,
801 potentially enhanced by spawning aggregation behavior. The aggregation factor increases
802 effective local density within spawning clumps above the spatially uniform average when
803 adult count exceeds a threshold.

804 This produces a quadratic relationship between zygote production and density at low
805 density: $\text{zygotes} \propto \rho_f \times \mathcal{F}(\rho_m) \propto \rho^2$ when $\rho \rightarrow 0$, creating a strong demographic Allee
806 effect. For high-fecundity broadcast spawners like *P. helianthoides*, the deterministic
807 Allee threshold is near zero density; the practical Allee effect operates through stochastic
808 processes at low N .

809 **5.7 Larval Phase**

810 Fertilized eggs enter a temperature-dependent pelagic larval duration (PLD):

$$\text{PLD}(T) = \text{PLD}_{\text{ref}} \cdot \exp(-Q_{\text{dev}} \cdot (T - T_{\text{ref}})) \quad (52)$$

811 where $\text{PLD}_{\text{ref}} = 63$ days at $T_{\text{ref}} = 10.5^\circ\text{C}$ [33], and $Q_{\text{dev}} = 0.05 \text{ } ^\circ\text{C}^{-1}$ produces shorter
812 PLD at warmer temperatures. PLD is clamped to $[30, 150]$ days.

813 Larval survival during the pelagic phase follows a constant daily mortality model:

$$S_{\text{larval}} = \exp(-\mu_{\text{larva}} \cdot \text{PLD}) \quad (53)$$

814 with $\mu_{\text{larva}} = 0.05 \text{ d}^{-1}$. At the reference PLD of 63 days, this yields $S_{\text{larval}} \approx 4.3\%$ — high
815 mortality that is compensated by the enormous fecundity of *P. helianthoides*.

816 Larval cohorts carry genotypes inherited via the SRS lottery (Section 4.5) and are
817 tracked as discrete objects during the pelagic phase. Upon completion of PLD, competent
818 larvae are available for settlement. In the spatial simulation (Section 6), cohorts are
819 dispersed between nodes via the larval connectivity matrix \mathbf{C} before settlement.

820 **5.8 Settlement and Recruitment**

821 Competent larvae settle into the benthic population through a three-stage process:

822 **1. Settlement cue (Allee effect).** Settlement success is modulated by the pres-
823 ence of conspecific adults via a Michaelis–Menten function representing biofilm-mediated
824 settlement cues:

$$C_{\text{settle}}(N_{\text{adults}}) = 0.2 + \frac{0.8 \cdot N_{\text{adults}}}{5 + N_{\text{adults}}} \quad (54)$$

825 where the baseline of 0.2 represents settlement on coralline algae in the absence of adults,
826 and the additional 0.8 reflects enhanced settlement induced by adult biofilm. The half-
827 saturation constant of 5 adults means that even a small remnant population provides
828 strong settlement cues.

829 **2. Density-dependent recruitment (Beverton–Holt).** The number of recruits is
830 governed by a standard Beverton–Holt stock-recruitment relationship:

$$R = \frac{K \cdot s_0 \cdot S}{K + s_0 \cdot S} \quad (55)$$

831 where S is the number of effective settlers (after cue modulation), K is the carrying
832 capacity, and $s_0 = 0.03$ is the density-independent per-settler survival rate. At low S ,

833 $R \approx s_0 S$ (supply-limited); at high S , $R \rightarrow K$ (habitat-limited). For broadcast spawners
834 with $S \gg K$, recruitment is typically habitat-limited and population self-regulates.

835 **3. Agent initialization.** Recruited settlers are placed in dead agent slots, assigned
836 size 0.5 mm, age 0, Settler stage, random sex (1:1 ratio), Susceptible disease state, and
837 random position within the node’s habitat area. Genotypes are copied from the SRS-
838 selected settler genotypes, and all three trait scores (r_i , t_i , c_i) are computed from the
839 inherited genotype.

840 **Juvenile immunity.** Newly settled individuals can optionally be granted a juvenile
841 immunity period (configurable, default 0 days) during which they are not susceptible
842 to infection. The settlement day is recorded for each recruit to enable age-dependent
843 susceptibility calculations.

844 5.9 Continuous Settlement

845 Rather than settling all larvae in an annual pulse, the model tracks individual larval
846 cohorts and settles them daily as their PLD elapses. Cohorts generated by daily spawning
847 events throughout the extended spawning season (Section 5.4.1) are stored in a per-node
848 pending list sorted by settlement day. Each simulation day, cohorts whose PLD has
849 elapsed are popped from the sorted list front (amortized $O(1)$) and passed through the
850 settlement pipeline. This continuous approach produces realistic seasonal recruitment
851 pulses that peak several months after the spawning peak, consistent with the observed
852 temporal offset between spawning and juvenile recruitment in *P. helianthoides*.

853 At the annual boundary, any remaining unsettled cohorts from each node are collected
854 for spatial dispersal via the connectivity matrix \mathbf{C} (Section 6), then redistributed to
855 destination nodes where they continue to settle daily as PLD elapses.

856 5.10 Demographic–Genetic–Epidemiological Coupling

857 The population dynamics module is bidirectionally coupled to the disease and genetics
858 modules:

- 859 • **Disease → demographics:** Disease kills individuals ($I_2 \rightarrow D$), reducing popula-
860 tion size and altering age/size structure. Post-spawning immunosuppression (Sec-
861 tion 5.4.4) increases disease risk for recent spawners, creating a temporal alignment
862 between peak reproductive effort and peak epidemic severity during warm months.
- 863 • **Demographics → disease:** Reduced population density lowers contact rates and
864 environmental pathogen concentration. The fertilization Allee effect (Section 5.6)

865 amplifies population collapse by reducing reproductive output at low density, po-
866 tentially trapping populations in an extinction vortex.

- 867 • **Genetics → demographics:** The SRS lottery (Section 4.5) produces extreme
868 reproductive variance that amplifies genetic drift while accelerating the fixation
869 of resistance, tolerance, and recovery alleles enriched by selection during epidemic
870 episodes.
- 871 • **Demographics → genetics:** Population bottlenecks from disease reduce N_e far
872 below census N , compounded by SRS ($N_e/N \sim 10^{-3}$). The interaction of selection
873 with small effective population size determines whether evolutionary rescue is fast
874 enough to prevent extinction.

875 6 Spatial Module and Environmental Forcing

876 SSWD-EvoEpi represents the NE Pacific range of *Pycnopodia helianthoides* as a metapop-
877 ulation network of discrete spatial nodes connected by larval dispersal and pathogen
878 transport. Each node carries its own environmental forcing (sea surface temperature,
879 salinity, flushing rate) that modulates local disease and demographic dynamics. This sec-
880 tion describes the spatial architecture, connectivity matrices, environmental time series,
881 and agent movement model.

882 6.1 Metapopulation Network Structure

883 The metapopulation is a graph $\mathcal{G} = (\mathcal{N}, \mathbf{C}, \mathbf{D})$ where each node $k \in \mathcal{N}$ represents a geo-
884 graphically delineated habitat patch and \mathbf{C} , \mathbf{D} are the larval and pathogen connectivity
885 matrices, respectively.

886 6.1.1 Node Definition

887 Each node is parameterized by a `NodeDefinition` record with the following fields:

Table 7: Node definition fields.

Field	Units	Description
lat, lon	°N, °E	Geographic coordinates
carrying_capacity	individuals	Local K ($=$ habitat area $\times \rho_{\max}$)
is_fjord	bool	Fjord vs. open coast classification
sill_depth	m	Sill depth (∞ for open coast)
flushing_rate	d $^{-1}$	Mean annual hydrodynamic flushing ϕ_k
mean_sst	°C	Baseline annual mean SST
sst_amplitude	°C	Annual cycle half-range
sst_trend	°C yr $^{-1}$	Linear warming trend
salinity	psu	Effective mean salinity
depth_range	m	Min–max habitat depth
subregion	—	Biogeographic subregion code

888 At runtime, each `NodeDefinition` is wrapped in a `SpatialNode` object that holds the
 889 local population arrays (agents and genotypes), current environmental state (SST, salin-
 890 ity, flushing rate), Vibrio concentration, and diagnostic flags. The `MetapopulationNetwork`
 891 aggregates all nodes together with the **C**, **D**, and distance matrices.

892 6.1.2 Internode Distance Computation

893 Connectivity kernels require pairwise waterway distances between nodes. Two methods
 894 are available:

895 **Haversine with tortuosity.** For small networks (≤ 11 nodes), geodesic great-circle
 896 distances are computed via the Haversine formula and multiplied by a uniform tortuosity
 897 factor $\tau = 1.5$ (intermediate between open-coast ~ 1.2 and fjord ~ 2.5) to approximate
 898 along-coast path lengths:

$$d_{jk}^{\text{water}} = \tau \times d_{jk}^{\text{Haversine}}. \quad (56)$$

899 **Precomputed overwater distances.** For full-range simulations, a 489-site overwater
 900 distance matrix was computed from GEBCO 2022 bathymetric data at 15 arc-second res-
 901 olution. Land cells were rasterized from Natural Earth 10 m land polygons, and Dijkstra's
 902 algorithm on a 4-connected ocean grid yielded shortest overwater paths. The resulting
 903 489×489 matrix spans 2.0–7,187 km, with 98.4% of pairs connected (1,946 disconnected
 904 pairs involve western Aleutian sites near the antimeridian). Model nodes are matched
 905 to the nearest precomputed site within a 50 km tolerance; unmatched nodes fall back to
 906 Haversine $\times \tau$.

907 6.2 Connectivity Matrices

908 Two connectivity matrices govern inter-node exchange: \mathbf{C} for annual larval dispersal and
 909 \mathbf{D} for daily pathogen transport (Errata E5). Both use exponential distance kernels but
 910 operate at different spatial and temporal scales.

911 6.2.1 Larval Connectivity Matrix \mathbf{C}

912 C_{jk} gives the probability that a competent larva produced at node j settles at node k . The
 913 matrix is constructed from an exponential dispersal kernel with explicit self-recruitment:

$$C_{jk} = \begin{cases} \alpha_j & \text{if } j = k, \\ (1 - \alpha_j) \exp\left(-\frac{d_{jk}}{D_L}\right) b_{jk} & \text{if } j \neq k, \end{cases} \quad (57)$$

914 where:

- 915 • $D_L = 400$ km is the larval dispersal length scale, reflecting the 4–8 week pelagic
 916 larval duration (PLD) of *Pycnopodia helianthoides* [?];
- 917 • α_j is the self-recruitment fraction: $\alpha_{\text{fjord}} = 0.30$ for fjord nodes (reflecting enhanced
 918 retention behind sills) and $\alpha_{\text{open}} = 0.10$ for open-coast nodes;
- 919 • $b_{jk} \in [0, 1]$ is an optional barrier attenuation factor for biogeographic breaks (e.g.,
 920 Cape Mendocino).

921 Rows are then normalized so that:

$$\sum_k C_{jk} = r_{\text{total}} = 0.02, \quad (58)$$

922 where r_{total} represents the total per-larva settlement success probability, accounting for
 923 the compounding losses of pelagic mortality, failed metamorphosis, and post-settlement
 924 predation.

925 The elevated self-recruitment fraction for fjord nodes ($\alpha_{\text{fjord}} = 3\alpha_{\text{open}}$) encodes the em-
 926 pirical observation that fjords act as larval retention zones [?]: sill-mediated circulation
 927 traps larvae near their natal site, reducing export to the open coast.

928 6.2.2 Pathogen Dispersal Matrix \mathbf{D}

929 D_{jk} gives the fraction of waterborne *Vibrio pectenicida* at node j that reaches node k per
 930 day. Pathogen dispersal operates at much shorter range than larval dispersal:

$$D_{jk} = \phi_j f_{\text{out}} \exp\left(-\frac{d_{jk}}{D_P}\right) S_{jk} \quad \text{for } d_{jk} \leq 50 \text{ km}, \quad (59)$$

931 where:

- 932 • $D_P = 15$ km is the pathogen dispersal scale (reflecting tidal-current transport);
933 • ϕ_j is the source node's flushing rate (d^{-1});
934 • $f_{\text{out}} = 0.2$ is the fraction of flushed water reaching neighboring sites;
935 • S_{jk} is the sill attenuation factor.

936 Pairs beyond $d_{jk} > 50$ km receive zero pathogen transfer. Total export from any node
937 is capped at its flushing rate: $\sum_k D_{jk} \leq \phi_j$.

938 **Sill attenuation.** Fjord sills impede pathogen exchange between basins. The attenu-
939 ation factor is computed from the minimum sill depth across the pair:

$$S_{jk} = \min \left(1, \left[\frac{\min(z_j^{\text{sill}}, z_k^{\text{sill}})}{\max(z_j^{\text{max}}, z_k^{\text{max}})} \right]^2 \right), \quad (60)$$

940 where z^{sill} is sill depth and z^{max} is maximum habitat depth. For open-coast nodes ($z^{\text{sill}} =$
941 ∞), $S_{jk} = 1$ (no attenuation). For Howe Sound (sill = 30 m, max depth = 100 m),
942 $S \approx 0.09$, reducing pathogen exchange by $\sim 91\%$.

943 6.2.3 Dispersal Dynamics

944 **Pathogen dispersal (daily).** At each timestep, the dispersal input to node k is:

$$\Delta P_k^{\text{dispersal}} = \sum_j D_{jk} P_j = (\mathbf{D}^\top \mathbf{P})_k, \quad (61)$$

945 which enters the Vibrio ODE (Eq. 17) as an additive source term.

946 **Larval dispersal (annual).** At the end of each reproductive season, competent larvae
947 from each source node are distributed to receiving nodes via \mathbf{C} . For source node j
948 producing n_j competent larvae: (i) a binomial draw $n_{\text{settle}} \sim \text{Bin}(n_j, \sum_k C_{jk})$ determines
949 total settlement; (ii) a multinomial draw allocates settlers across destinations proportional
950 to the conditional probabilities $C_{jk} / \sum_k C_{jk}$; (iii) settler genotypes are sampled with
951 replacement from the source pool.

952 6.3 Environmental Forcing

953 Each node receives a locally parameterized environmental forcing that drives disease
954 and demographic rates through temperature-dependent, salinity-dependent, and flushing-
955 dependent mechanisms.

956 **6.3.1 Sea Surface Temperature**

957 Daily SST at node k follows a sinusoidal annual cycle with a linear warming trend and
 958 optional stochastic perturbation:

$$T_k(d, y) = \underbrace{\bar{T}_k + \gamma_k(y - y_{\text{ref}})}_{\text{trend-adjusted mean}} + \underbrace{A_k \cos\left(\frac{2\pi(d - d_{\text{peak}})}{365}\right)}_{\text{annual cycle}}, \quad (62)$$

959 where:

- 960 • \bar{T}_k is the baseline annual mean SST ($^{\circ}\text{C}$) at reference year $y_{\text{ref}} = 2000$;
- 961 • A_k is the annual cycle half-range ($^{\circ}\text{C}$);
- 962 • γ_k is the linear warming rate ($^{\circ}\text{C yr}^{-1}$; default 0.02);
- 963 • $d_{\text{peak}} = 227$ (day of year \approx August 15) corresponds to the late-summer SST maxi-
 964 um characteristic of the NE Pacific.

965 The warming trend shifts the SST climatology upward over time, increasing both
 966 baseline *Vibrio* viability and the duration of the high-risk summer window. For the 5-
 967 node validation network, \bar{T}_k ranges from 8.0°C (Sitka) to 14.0°C (Monterey), producing
 968 a $\sim 6^{\circ}\text{C}$ latitudinal gradient consistent with satellite SST climatologies.

969 SST time series are precomputed at initialization via `make_sst_timeseries` and
 970 stored as dense 1-D arrays of shape $(n_{\text{years}} \times 365)$ for efficient daily lookup.

971 **6.3.2 Temperature-Dependent Rate Scaling**

972 All temperature-dependent biological rates—disease progression, pathogen shedding, *Vib-*
 973 *rio* decay—are scaled via the Arrhenius function:

$$k(T) = k_{\text{ref}} \exp\left[\frac{E_a}{R} \left(\frac{1}{T_{\text{ref}}} - \frac{1}{T}\right)\right], \quad (63)$$

974 with $T_{\text{ref}} = 293.15\text{ K}$ (20°C), the thermal optimum of *Vibrio pectenicida* [35]. This
 975 formulation ensures that the latitudinal SST gradient (Eq. 62) produces emergent north–
 976 south gradients in disease severity, matching the observed pattern of southward-increasing
 977 SSWD mortality during the 2013–2015 outbreak [? ?].

978 **6.3.3 Salinity Modifier**

979 Vibrio viability is suppressed at low salinities via a quadratic ramp (Eq. 7), reproduced
 980 here for completeness:

$$S_{\text{sal}} = \text{clip}\left(\left[\frac{S_k - S_{\text{min}}}{S_{\text{full}} - S_{\text{min}}}\right]^2, 0, 1\right), \quad S_{\text{min}} = 10 \text{ psu}, \quad S_{\text{full}} = 28 \text{ psu}. \quad (64)$$

981 Fjord nodes receive lower salinities (e.g., Howe Sound $S = 22$ psu due to freshwater
 982 runoff), yielding $S_{\text{sal}} = 0.44$ and reducing effective Vibrio viability by $\sim 56\%$ compared
 983 to open-coast nodes ($S \geq 30$ psu, $S_{\text{sal}} \geq 0.87$). This mechanism provides a partial
 984 explanation for fjord refugia observations [?].

985 **6.3.4 Flushing Rate**

986 Hydrodynamic flushing removes waterborne pathogen at rate ϕ_k (d^{-1}), entering the Vibrio
 987 ODE as the term $-\phi_k P_k$ (Eq. 17). Node-specific values span two orders of magnitude:

- 988 • Open coast: $\phi_k = 0.5\text{--}1.0 \text{ d}^{-1}$ (strong tidal and current flushing);
- 989 • Semi-enclosed bays: $\phi_k = 0.3 \text{ d}^{-1}$ (San Juan Islands);
- 990 • Fjords: $\phi_k = 0.007\text{--}0.05 \text{ d}^{-1}$ (Errata E3; sill restricts water exchange). Howe Sound
 991 is assigned $\phi_k = 0.03 \text{ d}^{-1}$.

992 Low flushing in fjords acts as a double-edged mechanism: it reduces the rate of
 993 pathogen removal (potentially increasing local Vibrio concentrations) but also reduces
 994 pathogen *export* to neighboring nodes via \mathbf{D} (Eq. 59), effectively isolating the fjord from
 995 regional epidemic dynamics.

996 Flushing rates are optionally modulated seasonally:

$$\phi_k(m) = \bar{\phi}_k \left[1 + A_\phi \cos\left(\frac{2\pi(m-5)}{12}\right) \right], \quad (65)$$

997 where m is the 0-indexed month, $A_\phi = 0.3$ for fjord nodes and $A_\phi = 0.2$ for open
 998 coast, with peak flushing in June ($m = 5$) corresponding to freshwater-driven estuarine
 999 circulation maxima.

1000 **6.4 Agent Movement**

1001 Within each node, agents move via a correlated random walk (CRW) that produces
1002 realistic small-scale spatial structure:

$$\theta(t + \Delta t) = \theta(t) + \mathcal{N}(0, \sigma_\theta^2), \quad (66)$$

$$x(t + \Delta t) = x(t) + v_i \cos \theta \Delta t, \quad (67)$$

$$y(t + \Delta t) = y(t) + v_i \sin \theta \Delta t, \quad (68)$$

1003 where $\sigma_\theta = 0.6$ rad is the turning-angle standard deviation, $v_i = v_{\text{base}} \times m_{\text{state}}$ is the
1004 disease-modified speed, and $\Delta t = 60$ min (hourly substeps, 24 per day). The base speed
1005 $v_{\text{base}} = 0.5 \text{ m min}^{-1}$ is consistent with undisturbed *Pycnopodia helianthoides* locomotion
1006 rates [?]. Disease state modifies speed: $m_S = m_E = 1.0$ (healthy), $m_{I_1} = 0.5$ (mild
1007 impairment), $m_{I_2} = 0.1$ (severe wasting), $m_D = 0.0$ (stationary carcass), $m_R = 1.0$
1008 (recovered).

1009 Agents are confined to a square habitat of side length $\sqrt{\text{habitat_area}}$ with elastic
1010 boundary reflection.

1011 **Spatial transmission.** When spatial transmission is enabled, each node's habitat is
1012 discretized into a grid with cell size $\Delta x = 20$ m. Infected agents deposit pathogen expo-
1013 sure proportional to their shedding rate into their grid cell, and two Gaussian diffusion
1014 passes (3×3 averaging) smooth the resulting density field. Susceptible agents then experi-
1015 ence locally elevated or reduced force of infection depending on their proximity to infected
1016 individuals, creating emergent disease clustering without modifying the node-level Vibrio
1017 ODE.

1018 **Sensitivity analysis substeps.** The full 24 hourly substeps per day incur $\sim 20 \times$ com-
1019 putational overhead. For sensitivity analysis runs (Section ??), movement is reduced to
1020 1 substep per day, which captures spatial mixing and aggregation effects at acceptable
1021 cost.

1022 **6.5 Network Configurations**

1023 Three network configurations are used across model development, validation, and sensi-
1024 tivity analysis.

1025 **6.5.1 5-Node Validation Network**

1026 The primary validation network spans the NE Pacific range with five nodes selected to
1027 represent key biogeographic contexts (Table 8):

Table 8: 5-node validation network configuration. SST parameters are baseline values at reference year 2000.

Node	Lat	Lon	\bar{T} (°C)	A (°C)	S (psu)	ϕ (d^{-1})
Sitka, AK	57.06	-135.34	8.0	3.5	32.0	0.80
Howe Sound, BC	49.52	-123.25	10.0	4.0	22.0	0.03
San Juan Is, WA	48.53	-123.02	10.0	4.0	30.0	0.30
Newport, OR	44.63	-124.05	12.0	3.0	33.0	1.00
Monterey, CA	36.62	-121.90	14.0	2.5	33.5	0.80

1028 Howe Sound is the sole fjord node (sill depth = 30 m, $\alpha_{self} = 0.30$); all others are open
 1029 coast ($\alpha_{self} = 0.10$). Node carrying capacities range from 400 (Howe Sound) to 1,000
 1030 (Sitka). This network reproduces three key empirical patterns: the north–south SSWD
 1031 mortality gradient, fjord protection, and the absence of recovery in southern populations
 1032 (Section 8).

1033 6.5.2 11-Node Sensitivity Analysis Network

1034 Sensitivity analysis Rounds 1–3 used a minimal 3-node network (Sitka, Howe Sound,
 1035 Monterey) with inter-node distances of 1,700+ km—far exceeding the larval dispersal
 1036 scale $D_L = 400$ km. Consequently, the spatial connectivity parameters (D_L , α_{self}) were
 1037 effectively untestable, as the exponential kernel $\exp(-1700/400) < 10^{-2}$ produced negligi-
 1038 gible inter-node exchange regardless of D_L values within the SA range.

1039 Round 4 introduced an 11-node stepping-stone chain with six additional intermediate
 1040 nodes (Table 9), reducing maximum inter-node spacing to ~ 452 km and ensuring that
 1041 D_L values within the SA range [100, 1,000] km produce meaningful variation in larval ex-
 1042 change (32–76% at adjacent-node distances of 110–452 km with the default $D_L = 400$ km).

Table 9: 11-node stepping-stone network for sensitivity analysis Round 4. All nodes have $K = 5,000$ ($\sim 55,000$ total agents). SST trend = $0.02^{\circ}\text{C yr}^{-1}$ for all nodes.

Node	Lat	Lon	\bar{T} ($^{\circ}\text{C}$)	A ($^{\circ}\text{C}$)	S (psu)	ϕ (d^{-1})
Sitka	57.06	-135.34	8.0	3.5	32.0	0.80
Ketchikan	55.34	-131.64	8.5	3.5	31.0	0.50
Haida Gwaii	53.25	-132.07	9.0	3.0	31.5	0.60
Bella Bella	52.16	-128.15	9.5	3.5	28.0	0.40
Howe Sound*	49.52	-123.25	10.0	4.0	22.0	0.03
SJI	48.53	-123.02	10.5	4.0	30.0	0.30
Westport	46.89	-124.10	11.0	3.5	32.0	0.50
Newport	44.63	-124.05	11.5	3.0	33.0	0.60
Crescent City	41.76	-124.20	12.0	2.5	33.0	0.50
Fort Bragg	39.45	-123.80	12.5	2.5	33.5	0.50
Monterey	36.62	-121.90	13.0	2.5	33.5	0.40

*Fjord node (sill depth = 30 m, $\alpha_{\text{self}} = 0.30$). All other nodes open coast ($\alpha_{\text{self}} = 0.10$).

1043 This upgrade substantially altered parameter importance rankings: $n_{\text{resistance}}$ rose from
 1044 rank 19 to rank 5 (the three-trait partition amplifies genetic architecture importance at
 1045 finer spatial scales), and $P_{\text{env},\text{max}}$ rose from rank 11 to rank 4 (the environmental reservoir
 1046 becomes critical with more nodes seeding independent epidemics). See Section ?? for full
 1047 results.

1048 6.5.3 Full-Range Network (Planned)

1049 Scaling analysis (Section 8) demonstrated that the model supports 150-node networks at
 1050 ~ 66 s per 20-year run, enabling a full NE Pacific coastline simulation (Alaska to Baja
 1051 California). This configuration will use the precomputed 489-site overwater distance
 1052 matrix (Section 6.1.2) and site-specific SST forcing from satellite climatologies.

1053 6.6 Network Construction

1054 The `build_network` function assembles the metapopulation from a list of node definitions
 1055 by: (i) computing the pairwise distance matrix (Haversine $\times \tau$ or precomputed overwater
 1056 distances); (ii) constructing **C** with per-node α_j values (α_{fjord} or α_{open}), the D_L kernel,
 1057 optional barrier factors, and row normalization to r_{total} ; (iii) constructing **D** with the D_P
 1058 kernel, flushing-rate modulation, sill attenuation, and the 50 km cutoff; and (iv) wrapping
 1059 each node definition in a `SpatialNode` with initialized environmental state. The function
 1060 accepts optional parameters for all kernel scales, self-recruitment fractions, and barrier
 1061 configurations, allowing the same codebase to serve validation, sensitivity analysis, and
 1062 full-range simulation.

1063 7 Sensitivity Analysis

1064 The SSWD-EvoEpi model contains 47 uncertain parameters spanning six modules: dis-
1065 ease transmission and progression (16 parameters), genetics and trait architecture (8),
1066 population dynamics (7), spawning biology (7), pathogen virulence evolution (6), and
1067 spatial connectivity (3). Most of these parameters have limited empirical constraints
1068 (Section A), necessitating a systematic sensitivity analysis (SA) to identify which param-
1069 eters most influence model behavior and, critically, which parameter *interactions* domi-
1070 nate the system’s dynamics. We conducted a progressive, four-round SA campaign that
1071 tracked the model’s growing complexity from a single-trait, 3-node prototype through to
1072 the full three-trait, 11-node eco-evolutionary framework.

1073 7.1 Methods

1074 7.1.1 Morris Elementary Effects Screening

1075 Each SA round began with Morris elementary effects screening [48], implemented via the
1076 SALib Python library [26]. The Morris method is a one-at-a-time (OAT) design in which
1077 each parameter is perturbed along r independent trajectories through the p -dimensional
1078 input space. For parameter x_i in trajectory j , the elementary effect is

$$d_{ij} = \frac{f(x_1, \dots, x_i + \Delta_i, \dots, x_p) - f(x_1, \dots, x_i, \dots, x_p)}{\Delta_i}, \quad (69)$$

1079 where Δ_i is the perturbation step. From these we compute two summary statistics per
1080 parameter per metric [8]:

- 1081 • μ_i^* : the mean of the *absolute* elementary effects, measuring overall parameter im-
1082 portance regardless of sign;
- 1083 • σ_i : the standard deviation of elementary effects, measuring interaction and nonlin-
1084 earity strength.

1085 When $\sigma_i/\mu_i^* > 1$, the parameter’s influence on the metric is dominated by interactions
1086 with other parameters rather than by its direct (additive) effect [53]. To enable cross-
1087 metric comparison, we normalize μ^* by the range of the metric across all trajectories,
1088 then rank parameters by the mean normalized μ^* across all output metrics.

1089 All rounds used $r = 20$ trajectories, yielding $r \times (p + 1)$ total model evaluations per
1090 round (e.g., $20 \times 48 = 960$ runs for the 47-parameter Round 4).

1091 7.1.2 Sobol Variance Decomposition

1092 Parameters surviving Morris screening advance to Sobol variance-based global sensitivity
1093 analysis [58], which decomposes the total output variance into contributions from individ-

1094 ual parameters and their interactions. Using the Saltelli sampling scheme [52], $N(2p + 2)$
1095 model evaluations produce two key indices for each parameter x_i and output metric Y :

- 1096 • $S_{1,i} = V_{x_i}[E_{x \sim i}(Y|x_i)] / V(Y)$: the *first-order* Sobol index, measuring the fraction
1097 of output variance attributable to x_i alone;
- 1098 • $S_{T,i} = 1 - V_{x \sim i}[E_{x_i}(Y|x \sim i)] / V(Y)$: the *total-order* index, capturing x_i 's contribu-
1099 tion including all interactions with other parameters.

1100 The gap $S_{T,i} - S_{1,i}$ quantifies the strength of parameter interactions. When $S_{T,i} \gg S_{1,i}$, the
1101 parameter's influence is mediated primarily through joint effects with other parameters,
1102 implying that it cannot be calibrated independently.

1103 7.1.3 Output Metrics

1104 The SA tracks 23 output metrics capturing demographic, evolutionary, spatial, and
1105 pathogen outcomes over 20-year simulations:

- 1106 • **Demographic:** population crash percentage, final population fraction, recovery
1107 (population returns to >50% of initial), extinction (metapopulation collapse), peak
1108 single-year mortality, time to population nadir, total disease deaths, disease death
1109 fraction;
- 1110 • **Evolutionary (host):** mean and maximum resistance shift ($\Delta\bar{r}$), tolerance shift
1111 ($\Delta\bar{t}$), recovery-trait shift ($\Delta\bar{c}$), additive variance retention ($V_A^{\text{post}}/V_A^{\text{pre}}$), evolution-
1112 ary rescue index (composite of survival and resistance gain), total recovery events,
1113 recovery rate;
- 1114 • **Spatial:** number of extinct nodes, north–south mortality gradient, fjord protection
1115 effect;
- 1116 • **Pathogen:** mean final virulence, virulence shift ($\Delta\bar{v}$);
- 1117 • **Spawning:** spawning participation rate, mean recruitment rate.

1118 7.2 Progressive Sensitivity Analysis Design

1119 The SA was conducted in four rounds (Table 10), each corresponding to a major model
1120 extension. This progressive design allows us to track how parameter importance shifts as
1121 model complexity grows—a critical diagnostic for identifying emergent behaviors intro-
1122 duced by new modules.

Table 10: Summary of sensitivity analysis rounds. Each round incorporates all changes from prior rounds. “New” parameters are those added relative to the previous round.

Round	Params	Metrics	Nodes	Runs	Key Changes
R1 (Morris)	23	14	3	480	Baseline: single resistance trait
R2 (Sobol)	23	14	3	12,288	Sobol decomposition of R1 params
R3 (Morris)	43	20	3	880	+20 params: pathogen evo, spawning, continuous mortality, daily growth
R4 (Morris)	47	23	11	960	+4 params: three-trait genetics, 11-node stepping-stone network

1123 **Rounds 1–2 (Pre-Three-Trait Baseline).** The initial SA (Rounds 1–2) examined
1124 23 parameters across disease (13), population (7), genetics (1: n_{additive}), and spawning
1125 (2) modules using a 3-node spatial network (Sitka, Howe Sound, Monterey; $K = 5,000$
1126 per node). The model at this stage tracked a single resistance trait with n_{additive} additive
1127 loci. Morris screening (480 runs) retained all 23 parameters for Sobol analysis (12,288
1128 runs, $N = 256$).

1129 The Sobol decomposition revealed that disease progression rate $\mu_{I2D,\text{ref}}$ ($I_2 \rightarrow \text{Death}$)
1130 was the single most influential parameter (mean $S_T = 0.638$), followed by susceptibility_multiplier
1131 ($S_T = 0.540$) and a_{exposure} ($S_T = 0.473$). A critical methodological finding was that Mor-
1132 ris and Sobol rankings *disagreed*: Morris identified `settler_survival` and ρ_{rec} as the
1133 top drivers of population outcomes, while Sobol elevated susceptibility_multiplier and
1134 $\mu_{I2D,\text{ref}}$. This discrepancy arises because Morris measures marginal effects from extreme-
1135 value perturbations, whereas Sobol captures variance-weighted contributions including
1136 interactions. This confirmed that Morris screening alone is insufficient for identifying
1137 calibration priorities in this model.

1138 **Round 3 (Expanded Model, 3-Node).** Round 3 added 20 parameters from four
1139 newly implemented modules: pathogen virulence evolution (6 parameters: virulence–
1140 fitness tradeoff exponents, mutation rate, initial virulence), expanded spawning biology
1141 (4: male spontaneous spawning, readiness induction, female bout limits, peak width), and
1142 additional disease mechanics (immunosuppression duration, minimum susceptible age,
1143 $I_1 \rightarrow I_2$ progression rate) and genetics parameters (target_mean_r, Beta-distribution
1144 shape parameters for initial allele frequencies). The network remained at 3 nodes for
1145 comparability with R1–R2.

1146 Morris screening (880 runs, 20 trajectories) revealed a dramatic reshuffling: ρ_{rec} (re-
1147 covery rate) rose to #1 ($\mu_{\text{norm}}^* = 0.642$), displacing $\mu_{I2D,\text{ref}}$ from its R1–R2 dominance.
1148 This occurred because the transition from discrete-stage to continuous daily mortality
1149 diluted the $I_2 \rightarrow \text{Death}$ rate’s marginal influence, while recovery rate’s role was amplified
1150 by its interaction with the new pathogen evolution module (higher ρ_{rec} imposes stronger
1151 selection against virulent strains). All 43 parameters exceeded the 5% elimination thresh-

1152 old; zero were pruned.

1153 **Round 4 (Full Model, 11-Node).** Round 4 represents the complete SSWD-EvoEpi
1154 model with two additions: (1) the three-trait genetic architecture (resistance, tolerance,
1155 recovery; Section 4.1), contributing four new parameters (`target_mean_c`, `target_mean_t`,
1156 τ_{\max} , $n_{tolerance}$); and (2) an 11-node stepping-stone network spanning the latitudinal range
1157 of *Pycnopodia helianthoides* habitat. The expanded spatial network was critical for re-
1158 solving spatial parameters that were undetectable at 3 nodes. This round (960 runs, 48
1159 cores on an Intel Xeon W-3365) provides the most comprehensive screening of the model
1160 to date.

1161 7.3 Round 4 Morris Results

1162 7.3.1 Global Parameter Ranking

1163 Table 12 presents the complete Round 4 Morris ranking for all 47 parameters, sorted by
1164 mean normalized μ^* across 23 output metrics. Figure 1 shows the top 20 parameters
1165 color-coded by module.

1166 The top-10 parameters span four of six modules:

- 1167 1. ρ_{rec} (recovery rate; $\mu_{\text{norm}}^* = 0.889$) — the rate at which infected individuals clear
1168 pathogen remains the single most influential parameter, as in R3. Its semi-additive
1169 behavior ($\sigma/\mu^* = 1.46$, the lowest interaction ratio of any parameter) reflects its
1170 direct mechanistic role: daily clearance probability $p_{\text{rec}} = \rho_{\text{rec}} \times c_i$ scales linearly
1171 with this rate regardless of other parameter values.
- 1172 2. k_{growth} (von Bertalanffy growth rate; $\mu_{\text{norm}}^* = 0.633$) — faster growth accelerates
1173 maturation and spawning eligibility, providing demographic compensation during
1174 epidemics. Rose from #5 (R3) to #2.
- 1175 3. K_{half} (half-infective dose; $\mu_{\text{norm}}^* = 0.622$) — the Michaelis–Menten saturation pa-
1176 rameter controlling infection probability. Rose from #8 to #3.
- 1177 4. $P_{\text{env,max}}$ (environmental reservoir; $\mu_{\text{norm}}^* = 0.598$) — background waterborne *V. pecteni-*
1178 *cida* input, independent of host shedding. Rose dramatically from #11 to #4,
1179 reflecting its interaction with the 11-node spatial network where environmental
1180 pathogen load varies with latitude and temperature.
- 1181 5. $n_{\text{resistance}}$ (number of resistance loci; $\mu_{\text{norm}}^* = 0.525$) — genetic architecture of re-
1182 sistance. The largest rank gain of any parameter: #19 → #5 ($\Delta = +14$). The
1183 three-trait partition (17 loci per trait vs. the former 51 total) amplifies the sensi-
1184 tivity to how many loci underlie each defense mechanism.

- 1185 6. s_0 (settler survival; $\mu_{\text{norm}}^* = 0.509$) — Beverton–Holt baseline recruitment. Dropped
 1186 modestly from #3 to #6.
- 1187 7. $\sigma_{2,\text{eff}}$ (late-stage shedding rate; $\mu_{\text{norm}}^* = 0.431$).
- 1188 8. $\mu_{I2D,\text{ref}}$ ($I_2 \rightarrow$ Death rate; $\mu_{\text{norm}}^* = 0.419$) — formerly the #1 parameter in R1–R2
 1189 Sobol ($S_T = 0.638$), now #8 in R4 Morris.
- 1190 9. σ_{spawn} (spawning peak width; $\mu_{\text{norm}}^* = 0.392$) — controls synchrony of the repro-
 1191 ductive pulse; dropped from #2 to #9.
- 1192 10. target_mean_c (initial mean recovery trait; $\mu_{\text{norm}}^* = 0.385$) — a new R4 parame-
 1193 ter entering directly at #10, confirming that the recovery trait (c_i) is the fastest-
 1194 evolving defense in the model (Section 4.1).

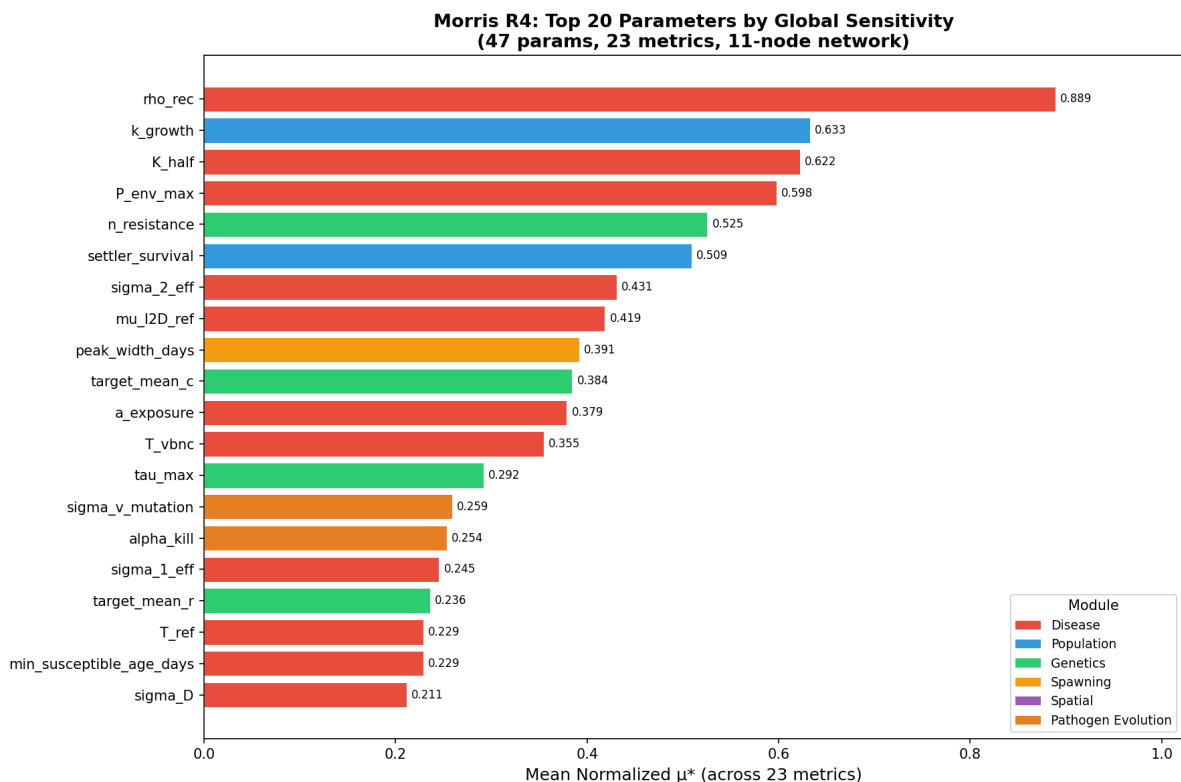


Figure 1: Top 20 parameters by mean normalized μ^* in Round 4 Morris screening (47 parameters, 23 metrics, 11-node network, 960 runs). Bars are color-coded by module. Error bars show 95% bootstrap confidence intervals across 20 trajectories.

1195 7.3.2 Key Rank Shifts from Round 3

1196 The transition from R3 to R4 produced dramatic rank changes (Figure 2), driven by two
 1197 structural changes: the three-trait genetic architecture and the 11-node spatial network.

₁₁₉₈ **Major rank gains.** Six parameters gained ≥ 7 ranks (Table 11):

- ₁₁₉₉ • $\sigma_{1,\text{eff}}$ (early shedding rate): #43 → #16 ($\Delta = +27$). Early shedding now interacts with pathogen evolution: σ_1 shapes the initial epidemic wave that determines the selection regime on virulence.
- ₁₂₀₂ • $\sigma_{v,\text{mut}}$ (virulence mutation step size): #31 → #14 ($\Delta = +17$). With 11 nodes providing diverse thermal and demographic environments, mutation rate controls how fast pathogen lineages adapt to local conditions.
- ₁₂₀₅ • T_{ref} (pathogen temperature optimum): #34 → #18 ($\Delta = +16$). The latitudinal temperature gradient across 11 nodes (vs. 3) amplifies the importance of the thermal reference point.
- ₁₂₀₈ • $n_{\text{resistance}}$: #19 → #5 ($\Delta = +14$), as discussed above.
- ₁₂₀₉ • $\alpha_{\text{self,open}}$ (open-coast larval retention): #39 → #25 ($\Delta = +14$). Spatial retention was invisible at 3 nodes but becomes detectable with 11 nodes and realistic dispersal distances.
- ₁₂₁₂ • $P_{\text{env,max}}$: #11 → #4 ($\Delta = +7$).

₁₂₁₃ **Major rank drops.** Five parameters dropped ≥ 19 ranks:

- ₁₂₁₄ • q_{init,β_b} (Beta-distribution shape b): #17 → #46 ($\Delta = -29$). Initial allele-frequency shape is overwhelmed by the trait-specific mean parameters (target_mean_r/t/c).
- ₁₂₁₆ • F_0 (reference fecundity): #20 → #47 ($\Delta = -27$). Diluted in the expanded 47-parameter space.
- ₁₂₁₈ • Immunosuppression duration: #15 → #42 ($\Delta = -27$). Its effect is absorbed by spawning parameters and the recovery trait (c_i), which provides an alternative pathway through immunosuppressed periods.
- ₁₂₂₁ • susceptibility_multiplier: #23 → #44 ($\Delta = -21$). This parameter was #1 in the R1–R2 Sobol analysis ($S_T = 0.540$); its precipitous decline reflects absorption by the explicit resistance genetics—individual r_i now captures susceptibility variation mechanistically, rendering the multiplicative modifier redundant.
- ₁₂₂₅ • p_{spont} , (female spontaneous spawning): #26 → #45 ($\Delta = -19$).

Morris R3→R4: Parameter Rank Changes
 (43 common params; R4 adds 4 new: n_tolerance, target_mean_t, target_mean_c, tau_max)

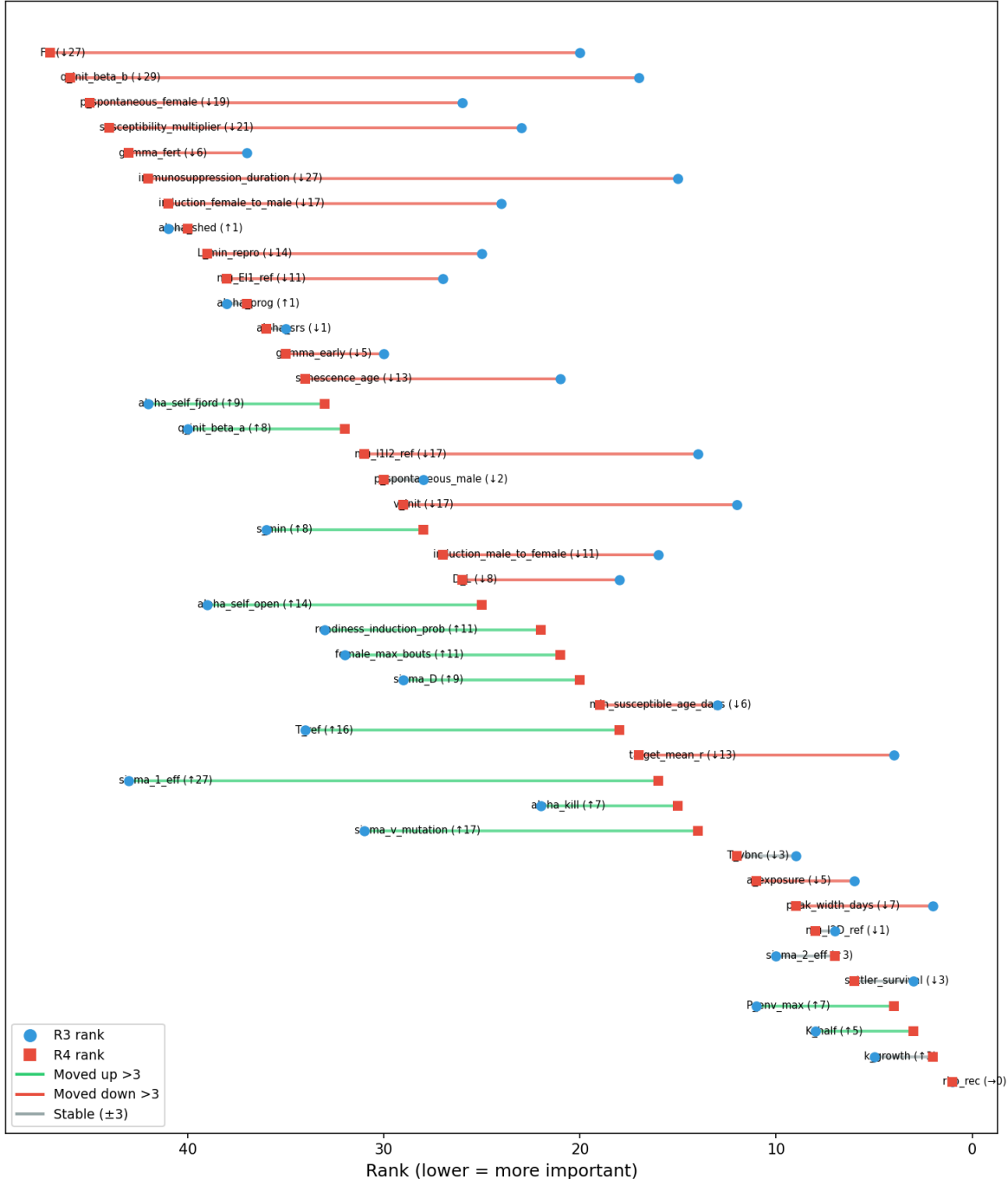


Figure 2: Rank change from Round 3 to Round 4 for the 43 parameters common to both rounds. Positive values (rightward) indicate increased importance in R4; negative values (leftward) indicate decreased importance. Parameters are sorted by R4 rank. Four new R4 parameters (not shown) entered at ranks #10, #13, #23, and #24.

Table 11: Largest rank shifts from R3 to R4 Morris screening. Positive Δ indicates increased importance.

Parameter	Module	R3 → R4	Δ	Mechanism
$\sigma_{1,\text{eff}}$	Disease	43 → 16	+27	Interacts with pathogen evolution
$\sigma_{v,\text{mut}}$	Pathogen evo.	31 → 14	+17	Controls adaptation speed
T_{ref}	Disease	34 → 18	+16	11-node thermal gradient
$n_{\text{resistance}}$	Genetics	19 → 5	+14	Three-trait partition
$\alpha_{\text{self,open}}$	Spatial	39 → 25	+14	Resolvable at 11 nodes
q_{init,β_b}	Genetics	17 → 46	-29	Absorbed by trait means
F_0	Population	20 → 47	-27	Diluted in larger space
Immunosupp. duration	Disease	15 → 42	-27	Absorbed by recovery trait
Suscept. multiplier	Disease	23 → 44	-21	Absorbed by resistance genetics

1226 7.3.3 New Three-Trait Parameters

1227 The four parameters introduced with the three-trait architecture (Section 4.1) immedi-
 1228 ately demonstrated meaningful sensitivity:

- 1229 • target_mean_c (initial mean recovery trait): rank #10 ($\mu_{\text{norm}}^* = 0.385$). A top-
 1230 10 entry confirms that recovery (c_i) is the dominant evolutionary pathway in the
 1231 model, consistent with the validation finding that $\Delta\bar{c}$ exceeds $\Delta\bar{r}$ by $\sim 7\times$ at all
 1232 nodes (Section 8).
- 1233 • τ_{max} (maximum tolerance scaling): rank #13 ($\mu_{\text{norm}}^* = 0.292$). The ceiling on how
 1234 much tolerance extends I_2 survival matters because it sets the upper bound on the
 1235 tolerance–recovery interaction.
- 1236 • target_mean_t (initial mean tolerance): rank #23 ($\mu_{\text{norm}}^* = 0.197$). Mid-pack,
 1237 reflecting the weaker selection signal on tolerance compared to recovery.
- 1238 • $n_{\text{tolerance}}$ (number of tolerance loci): rank #24 ($\mu_{\text{norm}}^* = 0.189$). Mid-pack, but no-
 1239 tably the most interacting parameter in the entire model ($\sigma/\mu^* = 2.51$), suggesting
 1240 tolerance’s role is context-dependent.

1241 7.3.4 Universal Nonlinearity

1242 A striking finding of the R4 Morris analysis is that *every one of the 47 parameters* has
 1243 $\sigma/\mu^* > 1.0$ (Figure 3). This means that no parameter in the model acts additively—every
 1244 parameter’s effect on every metric depends on the values of other parameters. The model
 1245 is a deeply coupled, nonlinear system.

1246 The interaction ratio σ/μ^* ranges from 1.42 (s_0 , settler survival) to 2.52 ($\sigma_{v,\text{mut}}$,
 1247 virulence mutation rate). Two interaction tiers are apparent:

- **Moderately interacting** ($\sigma/\mu^* < 1.5$; 2 parameters): ρ_{rec} (1.46) and s_0 (1.42). These parameters operate semi-additively—their effects are relatively stable across parameter space. For ρ_{rec} , this reflects its direct mechanistic role: daily clearance probability scales linearly with recovery rate regardless of context.
 - **Strongly to extremely interacting** ($\sigma/\mu^* > 1.5$; 45 parameters): the remaining parameters exhibit moderate to extreme nonlinearity. The most interacting parameters are genetic/evolutionary: $\sigma_{v,\text{mut}}$ (2.52), $n_{\text{tolerance}}$ (2.51), q_{init,β_a} (2.45), and α_{SRS} (2.34). These control *adaptation rates* that feed back on disease dynamics, which feed back on selection pressures—creating cascading interaction loops.

This universal nonlinearity has profound implications for calibration: no parameter can be tuned independently. Joint calibration via approximate Bayesian computation (ABC) or Markov chain Monte Carlo methods is essential.

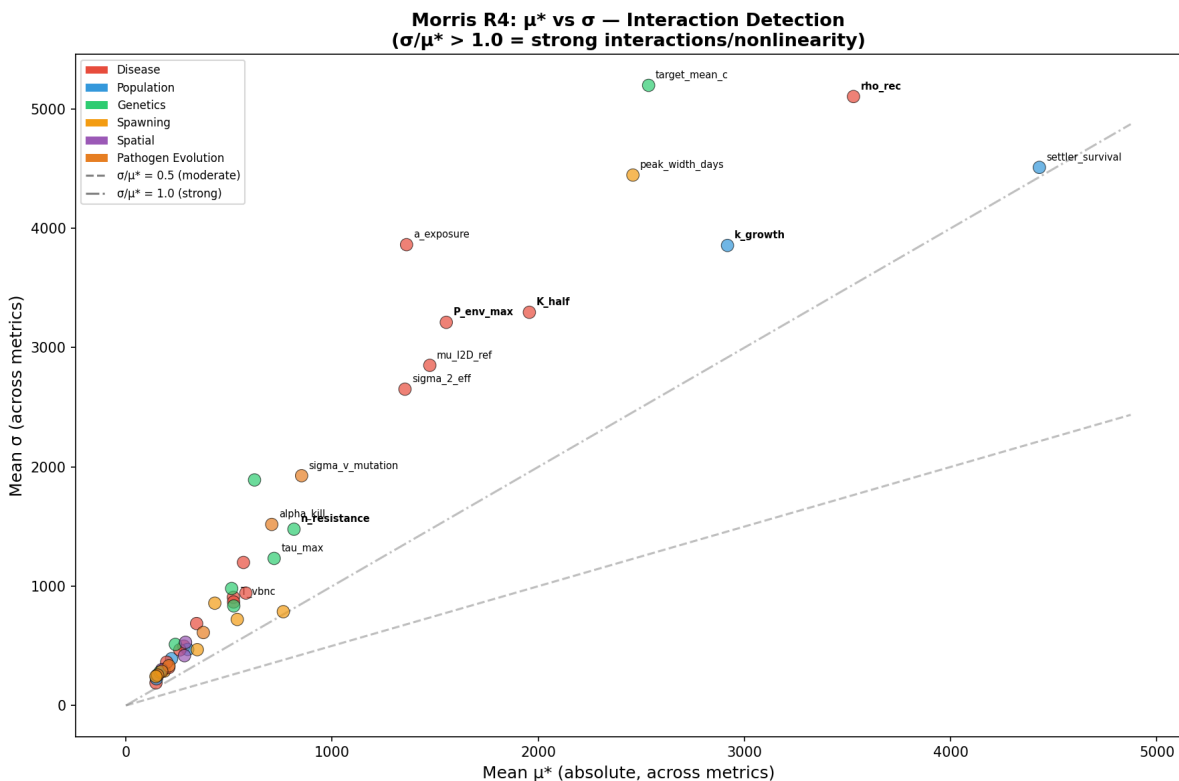


Figure 3: Morris μ^* vs. σ scatter for all 47 parameters (R4). The dashed line shows $\sigma = \mu^*$ (unit interaction ratio). All parameters fall above this line, indicating universal nonlinearity. Symbol color indicates module; symbol size scales with mean normalized μ^* .

7.3.5 Module-Level Sensitivity

Figure 4 summarizes sensitivity by module. The disease module dominates in both parameter count (16) and mean importance ($\overline{\mu_{\text{norm}}^*} = 0.332$), but genetics punches above

its weight: with only 8 parameters, it achieves the second-highest mean importance ($\overline{\mu_{\text{norm}}^*} = 0.260$), and its top parameter ($n_{\text{resistance}}$) ranks #5 globally. The pathogen evolution module, despite being entirely new in R3–R4, achieves a mean $\mu_{\text{norm}}^* = 0.185$ with $\sigma_{v,\text{mut}}$ at #14—virulence evolution is not negligible and must be retained in calibration.

Spatial parameters ($\overline{\mu_{\text{norm}}^*} = 0.171$) are detectable for the first time at 11 nodes. At the 3-node configuration of R1–R3, these parameters ranked #39–#42; at 11 nodes, they rise to #25–#33. This confirms that adequate spatial resolution is necessary to capture dispersal and retention dynamics.

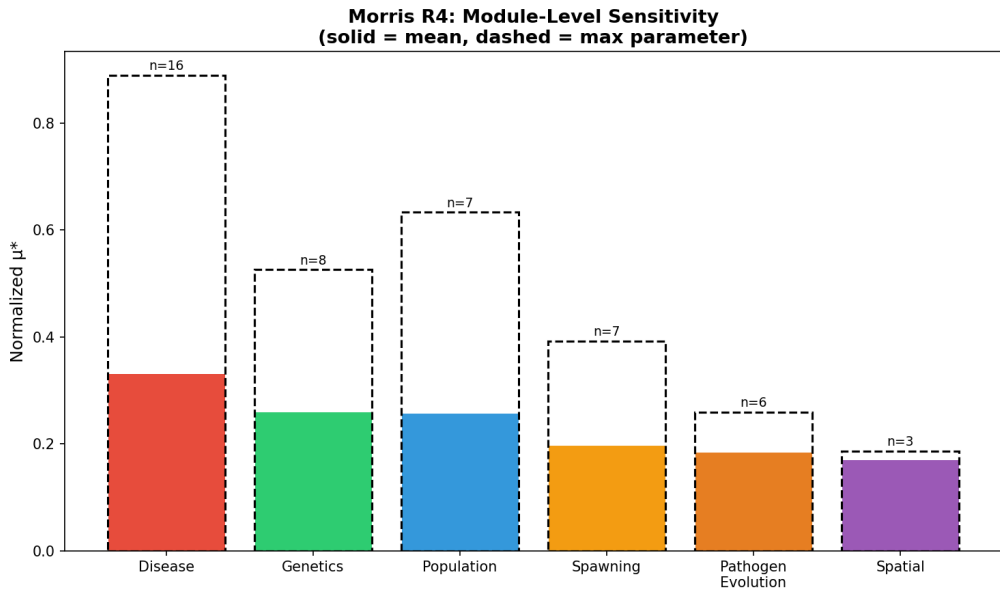


Figure 4: Module-level sensitivity summary for R4 Morris screening. Bar height shows mean normalized μ^* for each module; whiskers show the range from minimum to maximum parameter within each module. Number of parameters per module shown in parentheses.

7.4 Cross-Round Parameter Trajectories

Tracking individual parameters across all four rounds reveals which parameters have stable importance versus those whose influence is contingent on model structure (Figure 5):

Consistently important. ρ_{rec} , a_{exposure} , and $\sigma_{2,\text{eff}}$ remain in the top 12 across all rounds. These are robust calibration targets regardless of model configuration.

Structurally contingent. $\mu_{\text{I2D,ref}}$ was #1 in R1–R2 Sobol but dropped to #7–#8 in R3–R4 Morris after the switch to continuous daily mortality. `susceptibility_multiplier` fell from #1–#2 (R1–R2) to #44 (R4) as explicit resistance genetics absorbed its role. These shifts demonstrate that parameter importance can be an *artifact of model structure*,

not a property of the underlying biology, underscoring the need for structural sensitivity analysis alongside parametric SA.

Emergent with complexity. $P_{\text{env},\text{max}}$, $n_{\text{resistance}}$, and all pathogen evolution parameters only revealed their importance at ≥ 11 nodes or ≥ 43 parameters. Simple model configurations systematically underestimate the importance of spatial and evolutionary parameters.

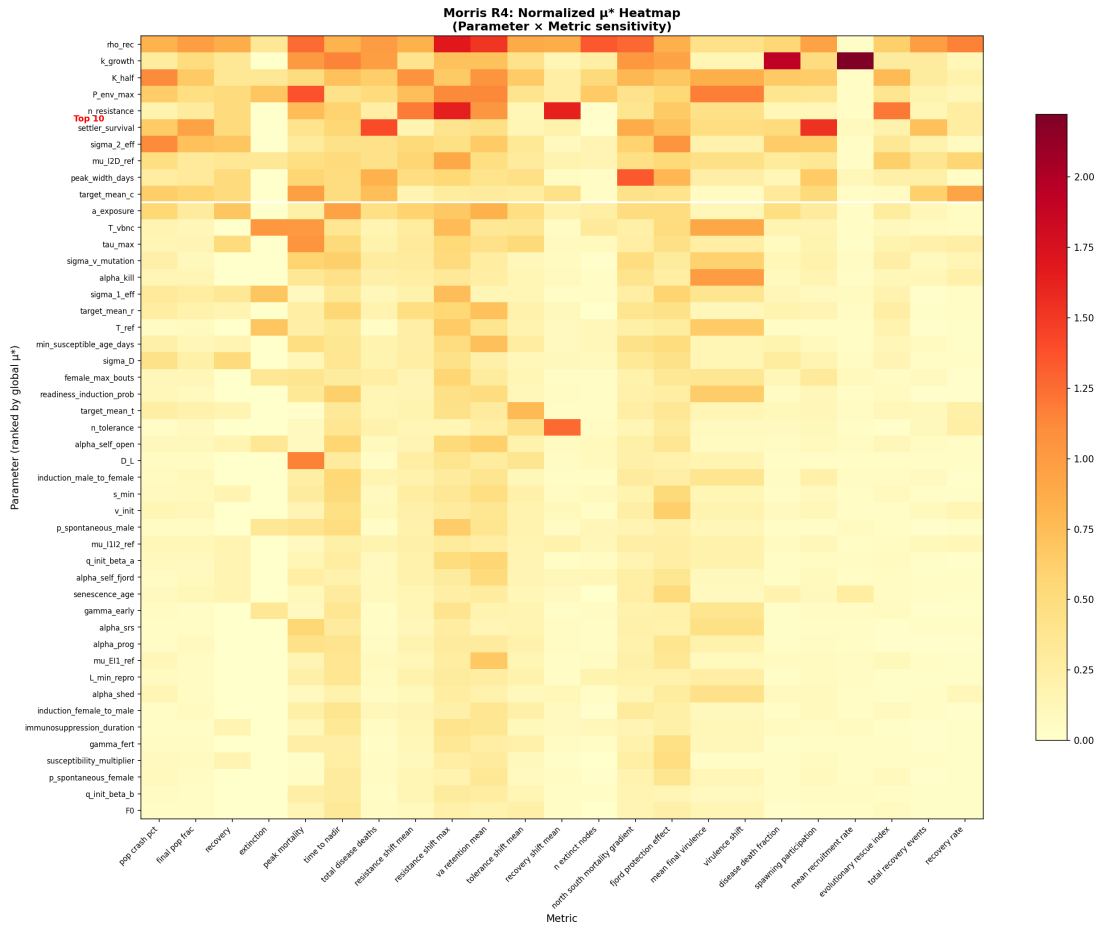


Figure 5: Parameter–metric sensitivity heatmap (R4 Morris). Cell color indicates normalized μ^* for each parameter–metric pair. Parameters (rows) are sorted by global rank; metrics (columns) are grouped by category. White cells indicate $\mu_{\text{norm}}^* < 0.05$.

1286 7.5 Sobol Variance Decomposition: Rounds 1–2 and Ongoing

1287 7.5.1 R1–R2 Sobol Results

1288 The Round 1–2 Sobol analysis (23 parameters, $N = 256$, 12,288 runs) revealed massive
 1289 parameter interactions across the model. For most metrics, total-order indices S_T far
 1290 exceeded first-order indices S_1 , meaning that parameter combinations dominate behavior
 1291 over individual effects. Notable interaction signatures include:

- **Extinction:** $\sigma_{2,\text{eff}}$ had $S_T = 1.51$ but $S_1 \approx 0$ —extinction risk is *entirely* driven by interactions between shedding rate and other parameters.
- **Fjord protection:** a_{exposure} had $S_T = 0.96$ but $S_1 = -0.12$ —a negative first-order index means the parameter’s effect *reverses sign* depending on the values of other parameters.
- **Recovery:** `susceptibility_multiplier` had $S_T = 0.96$ but $S_1 = 0.38$ —60% of its influence arises through interactions.

7.5.2 Round 4 Sobol (In Progress)

A Round 4 Sobol analysis is currently running on a 48-core Intel Xeon W-3365 server. With 47 parameters and $N = 512$, the Saltelli design requires $N(2p + 2) = 49,152$ model evaluations at ~ 25 s each. At 12 parallel workers, the estimated wall time is approximately 7 days. This analysis will provide the first variance decomposition of the full three-trait, 11-node model and will enable direct comparison with the R1–R2 Sobol indices to quantify how the three-trait architecture redistributes variance among parameters.

Based on the R4 Morris results, we prioritize convergence monitoring for the top-10 parameters and anticipate particularly informative second-order (S_2) indices for the following parameter pairs:

- $\rho_{\text{rec}} \times \text{target_mean_c}$: recovery rate \times recovery genetics (both affect pathogen clearance);
- $P_{\text{env,max}} \times a_{\text{exposure}}$: environmental reservoir \times transmission rate (dual exposure pathways);
- $n_{\text{resistance}} \times \sigma_{v,\text{mut}}$: host genetic architecture \times pathogen adaptation rate (coevolutionary arms race);
- $k_{\text{growth}} \times s_0$: growth rate \times recruitment (demographic compensation).

7.6 Summary and Implications

The four-round sensitivity analysis yields five principal findings:

1. **Recovery dominates.** The base recovery rate ρ_{rec} is consistently the most influential parameter across rounds and model configurations, yet has zero empirical basis. Determining whether *Pycnopodia helianthoides* can clear *V. pectenicia* infections—and at what rate—is the single highest-priority empirical question for model calibration.

- 1324 2. **Genetic architecture is a structural choice with major consequences.** The
1325 number of resistance loci ($n_{\text{resistance}}$) ranks #5 globally and cannot be calibrated
1326 from data without high-resolution GWAS. The three-trait partition amplifies this
1327 sensitivity: 17 loci per trait behave very differently from 51 loci in a single trait.
- 1328 3. **Parameter importance is model-contingent.** `susceptibility_multiplier` fell
1329 from #1 (R1–R2 Sobol) to #44 (R4 Morris) as explicit genetics absorbed its role;
1330 $\mu_{\text{I2D,ref}}$ fell from #1 to #8 with continuous mortality. SA results from simpler model
1331 configurations cannot be extrapolated to the full model.
- 1332 4. **Universal nonlinearity demands joint calibration.** All 47 parameters interact
1333 ($\sigma/\mu^* > 1.0$). No parameter can be tuned independently. Approximate Bayesian
1334 computation with sequential Monte Carlo sampling (ABC-SMC) is the appropriate
1335 calibration framework.
- 1336 5. **Spatial resolution matters.** Spatial and environmental parameters only emerge
1337 as important at ≥ 11 nodes. The planned 150-node full-coastline simulation will
1338 likely reveal additional spatially contingent sensitivities.

Table 12: Complete Round 4 Morris parameter ranking (47 parameters, 23 metrics, 11-node network, 960 runs). Mean normalized μ^* is averaged across all metrics. The σ/μ^* ratio indicates interaction strength (> 1 : interaction-dominated). R3 Rank column shows the parameter’s position in the 43-parameter R3 analysis; “—” indicates a new R4 parameter.

Rank	Parameter	Module	$\overline{\mu_{\text{norm}}^*}$	σ/μ^*	R3	Δ
1	ρ_{rec}	Disease	0.889	1.46	1	—
2	k_{growth}	Population	0.633	1.63	5	$\uparrow 3$
3	K_{half}	Disease	0.622	1.84	8	$\uparrow 5$
4	$P_{\text{env,max}}$	Disease	0.598	1.92	11	$\uparrow 7$
5	$n_{\text{resistance}}$	Genetics	0.525	1.78	19	$\uparrow 14$
6	s_0 (settler survival)	Population	0.509	1.42	3	$\downarrow 3$
7	$\sigma_{2,\text{eff}}$	Disease	0.431	1.95	10	$\uparrow 3$
8	$\mu_{\text{I2D,ref}}$	Disease	0.419	1.98	7	$\downarrow 1$
9	σ_{spawn} (peak width)	Spawning	0.392	2.03	2	$\downarrow 7$
10	target_mean_c	Genetics	0.385	2.08	—	—
11	a_{exposure}	Disease	0.379	2.20	6	$\downarrow 5$
12	T_{VBNC}	Disease	0.355	2.07	9	$\downarrow 3$
13	τ_{max}	Genetics	0.292	2.05	—	—
14	$\sigma_{v,\text{mut}}$	Path. evo.	0.259	2.52	31	$\uparrow 17$
15	α_{kill}	Path. evo.	0.254	2.25	22	$\uparrow 7$
16	$\sigma_{1,\text{eff}}$	Disease	0.245	2.24	43	$\uparrow 27$
17	target_mean_r	Genetics	0.236	1.86	4	$\downarrow 13$
18	T_{ref}	Disease	0.229	1.94	34	$\uparrow 16$
19	min. susceptible age	Disease	0.229	2.04	13	$\downarrow 6$

Continued on next page

Table 12 (continued)

Rank	Parameter	Module	$\overline{\mu_{\text{norm}}^*}$	σ/μ^*	R3	Δ
20	σ_D	Disease	0.211	1.96	29	$\uparrow 9$
21	female max bouts	Spawning	0.206	1.95	32	$\uparrow 11$
22	readiness induction prob.	Spawning	0.204	2.26	33	$\uparrow 11$
23	target_mean_t	Genetics	0.197	2.05	—	—
24	$n_{\text{tolerance}}$	Genetics	0.189	2.51	—	—
25	$\alpha_{\text{self,open}}$	Spatial	0.187	2.07	39	$\uparrow 14$
26	D_L	Spatial	0.178	2.29	18	$\downarrow 8$
27	κ_{mf} (M→F induction)	Spawning	0.176	2.07	16	$\downarrow 11$
28	s_{\min}	Disease	0.175	1.84	36	$\uparrow 8$
29	v_{init}	Path. evo.	0.173	2.13	12	$\downarrow 17$
30	$p_{\text{spont,m}}$	Spawning	0.169	2.11	28	$\downarrow 2$
31	$\mu_{\text{I1I2,ref}}$	Disease	0.156	1.97	14	$\downarrow 17$
32	q_{init,β_a}	Genetics	0.150	2.45	40	$\uparrow 8$
33	$\alpha_{\text{self,fjord}}$	Spatial	0.149	2.00	42	$\uparrow 9$
34	senescence age	Population	0.148	1.66	21	$\downarrow 13$
35	γ_{early}	Path. evo.	0.148	2.03	30	$\downarrow 5$
36	α_{SRS}	Population	0.146	2.34	35	$\downarrow 1$
37	α_{prog}	Path. evo.	0.143	2.09	38	$\uparrow 1$
38	$\mu_{\text{EI1,ref}}$	Disease	0.141	2.19	27	$\downarrow 11$
39	$L_{\min,\text{repro}}$	Population	0.139	2.06	25	$\downarrow 14$
40	α_{shed}	Path. evo.	0.136	2.12	41	$\uparrow 1$

Continued on next page

Table 12 (continued)

Rank	Parameter	Module	$\overline{\mu_{\text{norm}}^*}$	σ/μ^*	R3	Δ
41	κ_{fm} (F→M induction)	Spawning	0.130	1.79	24	↓17
42	immunosupp. duration	Disease	0.127	2.07	15	↓27
43	γ_{fert}	Population	0.122	2.21	37	↓6
44	suscept. multiplier	Disease	0.111	2.03	23	↓21
45	$p_{\text{spont,f}}$	Spawning	0.110	1.67	26	↓19
46	q_{init,β_b}	Genetics	0.104	2.20	17	↓29
47	F_0	Population	0.102	1.83	20	↓27

1339 **8 Validation**

1340 We validate the SSWD-EvoEpi model through a two-stage strategy: calibration and
 1341 behavioral verification at computationally cheap population sizes ($K = 5,000$ per node,
 1342 $\sim 25,000$ total agents), followed by scale-up validation at ecologically realistic population
 1343 sizes ($K = 100,000$ per node, 500,000 total agents). This approach tests whether emergent
 1344 dynamics—trait evolution trajectories, spatial mortality gradients, and extinction vortex
 1345 behavior—are robust to a 20-fold increase in population size, or whether they are artifacts
 1346 of stochastic fluctuations in small populations. All validation runs use a 5-node stepping-
 1347 stone network (Sitka, Howe Sound, San Juan Islands, Newport, Monterey), a 20-year
 1348 time horizon with disease introduction at year 3, seed 42, and the three-trait genetic
 1349 architecture described in Section 4.1 (17 resistance / 17 tolerance / 17 recovery loci).

1350 **8.1 $K = 5,000$ Validation**

1351 The small-population validation serves as the primary calibration target, permitting rapid
 1352 iteration (~ 108 s per 20-year simulation) while retaining sufficient genetic variance for
 1353 trait-level dynamics to emerge. Table 13 reports per-node demographic and evolutionary
 1354 outcomes.

Table 13: Per-node results for the $K = 5,000$ validation run (5 nodes, 20 years, seed 42). Δr_i , Δt_i , and Δc_i denote changes in mean resistance, tolerance, and recovery trait scores relative to initialization ($\bar{r}_0 = 0.15$, $\bar{t}_0 = 0.10$, $\bar{c}_0 = 0.02$). Pop_{min} gives the minimum population reached at the indicated year.

Node	N_0	N_{20}	N_{\min} (yr)	Crash	Deaths	Rec.	Δr_i	Δt_i	Δc_i
Sitka	4,935	65	65 (19)	98.7%	7,409	60	+0.011	+0.005	+0.029
Howe Sound	4,937	60	60 (19)	98.8%	9,473	55	-0.002	+0.044	+0.041
SJI	4,918	50	50 (13)	99.0%	7,985	63	+0.012	-0.007	+0.072
Newport	4,998	27	27 (17)	99.5%	7,918	51	+0.031	+0.001	+0.054
Monterey	5,000	163	38 (10)	99.2%	9,183	136	+0.025	+0.027	+0.154
Total	24,788	365		98.5%	41,968	365			

1355 Several key patterns emerge from the small-population run:

1356 **Severe, universal population crashes.** All five nodes experience >98% popula-
 1357 tion decline over 17 years of active disease, with total metapopulation crash of 98.5%
 1358 (24,788 \rightarrow 365 individuals). No node recovers to pre-epidemic levels, consistent with
 1359 the persistent absence of *Pycnopodia helianthoides* across most of its former range since
 1360 2013–2015 [19, 22].

1361 **Differential recovery at Monterey.** Monterey exhibits a distinctive trajectory: the
1362 population crashes to a minimum of 38 individuals at year 10 but partially rebounds to
1363 163 by year 20, driven by 136 disease recoveries— $2.2 \times$ the next-highest node (SJI, 63
1364 recoveries). This node also shows the strongest evolutionary signal in recovery ($\Delta c_i =$
1365 $+0.154$), consistent with warmer temperatures driving both higher disease pressure and
1366 stronger selection for clearance ability.

1367 **Recovery is the fastest-evolving trait.** Across all five nodes, the mean change in
1368 recovery trait score ($\overline{\Delta c_i} = +0.070$) exceeds that of resistance ($\overline{\Delta r_i} = +0.015$) by $4.5 \times$ and
1369 tolerance ($\overline{\Delta t_i} = +0.014$) by $5.0 \times$ (Table 13). This asymmetry arises because recovery
1370 acts as a multiplicative modifier on the daily probability of transitioning from infected
1371 to recovered ($p_{\text{rec}} = \rho_{\text{rec}} \times c_i$; Section 3), creating strong directional selection: individuals
1372 with higher c_i survive infection and contribute disproportionately to the next generation.

1373 **Resistance signal is weak and mixed.** With only 17 loci encoding resistance (com-
1374 pared to 51 in the original single-trait architecture), the per-locus allele frequency shifts
1375 are small ($\Delta q \approx 0.001$ – 0.004). Three of five nodes show positive Δr_i (Sitka, SJI, New-
1376port), but Howe Sound shows a negligible decline (-0.002), consistent with genetic drift
1377 overwhelming weak directional selection at small effective population sizes [25].

1378 **Tolerance is effectively neutral.** Mean tolerance change is negligible ($\overline{\Delta t_i} = +0.014$),
1379 with one node showing a slight decrease (SJI, $\Delta t_i = -0.007$). This is expected: tolerance
1380 extends survival time during late infection (I_2) via timer-scaling (Section 3), but this
1381 effect is weak when recovery rates are low and late-stage mortality is high. Tolerance
1382 becomes selectively relevant only when disease mortality is moderated by other mech-
1383anisms, creating a conditional neutrality that limits its evolutionary response under severe
1384 epidemic conditions.

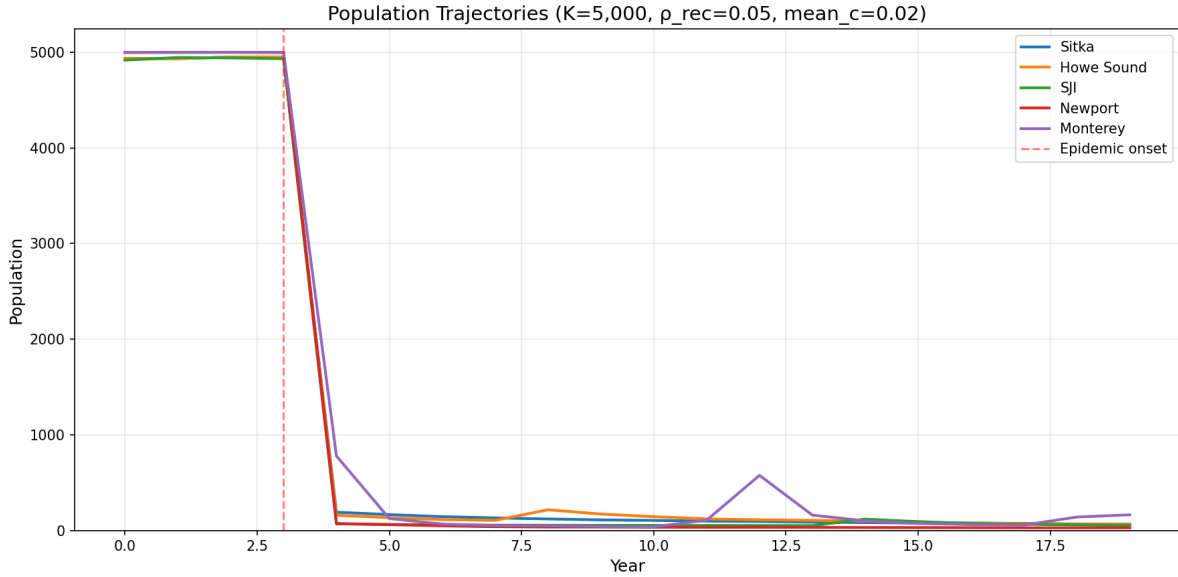


Figure 6: Population trajectories for the $K = 5,000$ validation run. Disease is introduced at year 3. All nodes crash to $<2\%$ of carrying capacity. Monterey (red) shows partial recovery from its nadir of 38 individuals at year 10, driven by elevated recovery trait evolution ($\Delta c_i = +0.154$).

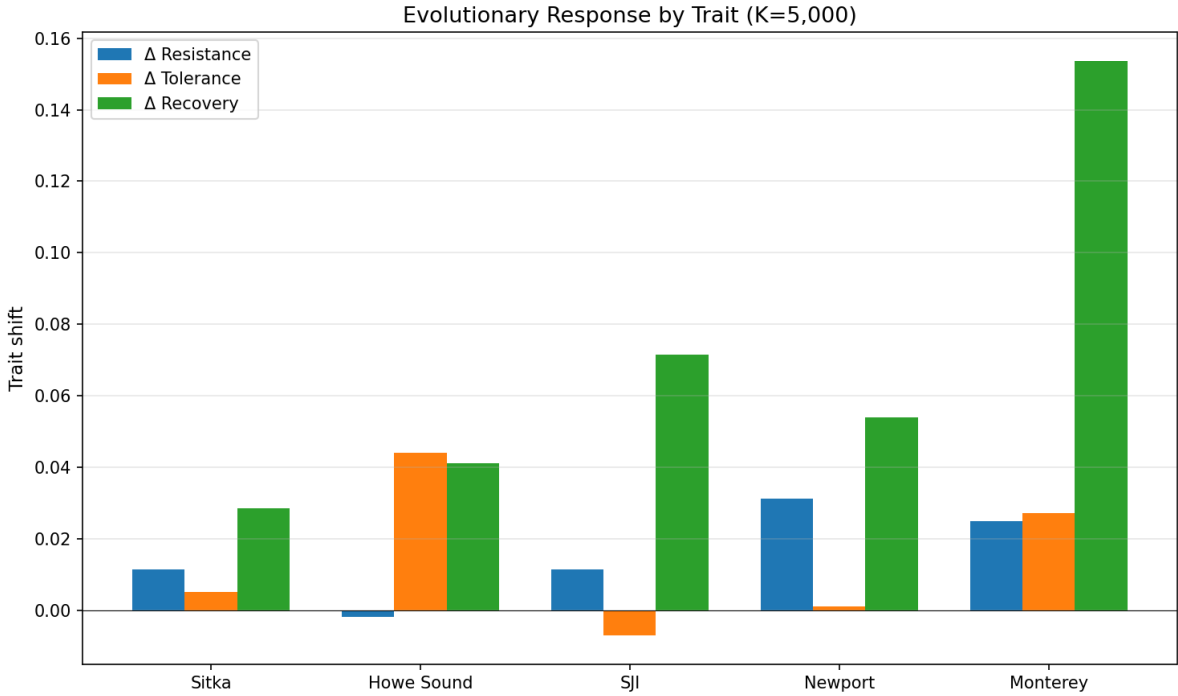


Figure 7: Trait shifts (Δr_i , Δt_i , Δc_i) per node in the $K = 5,000$ validation. Recovery (blue) dominates at every node, with Monterey showing the largest shift ($\Delta c_i = +0.154$). Resistance changes are weak and variable in sign; tolerance is near-zero at most nodes.

1385 8.2 $K = 100,000$ Scale-Up Validation

1386 To test whether patterns observed at $K = 5,000$ persist at ecologically realistic population
 1387 sizes, we scale carrying capacity 20-fold to $K = 100,000$ per node (500,000 total agents).
 1388 This run required 42.6 minutes (2,558 s) and ~ 1.5 GB peak memory, compared to 108 s
 1389 for the small-population equivalent—a $23.7\times$ slowdown that is sublinear relative to the
 1390 $20\times$ population increase, consistent with the $O(N^{0.62})$ scaling relationship established in
 1391 Section 7.1. Table 14 reports the results.

Table 14: Per-node results for the $K = 100,000$ scale-up validation (5 nodes, 20 years, seed 42). Trait values are final means; Δ values computed relative to initialization targets ($\bar{r}_0 = 0.15$, $\bar{t}_0 = 0.10$, $\bar{c}_0 = 0.02$).

Node	N_{20}	Crash	Deaths	Rec.	Δr_i	Δt_i	Δc_i
Sitka	718	99.3%	109,151	875	-0.004	+0.002	+0.059
Howe Sound	633	99.4%	112,112	913	-0.004	+0.008	+0.056
SJI	733	99.3%	108,607	916	-0.009	+0.010	+0.060
Newport	639	99.4%	110,563	922	-0.005	+0.006	+0.065
Monterey	2,904	97.1%	125,061	1,319	-0.002	+0.000	+0.075
Total	5,627	98.9%	565,494	4,945			

1392 The scale-up validation reveals several important findings:

1393 **Crashes are worse, not better, at larger N .** Total metapopulation crash increases
 1394 from 98.5% at $K = 5,000$ to 98.9% at $K = 100,000$ (Table 15). This counterintuitive
 1395 result refutes the hypothesis that larger populations buffer against extinction through
 1396 stochastic rescue. In the SSWD-EvoEpi framework, larger populations sustain higher ab-
 1397 solute disease transmission (more contacts per susceptible per day) while the per-capita
 1398 selection intensity remains constant, meaning that deterministic epidemic dynamics dom-
 1399 inate and demographic stochasticity—which occasionally permits small populations to
 1400 “escape” the disease through random fluctuations—is suppressed. The 0.4 percentage-
 1401 point increase in crash severity is small but directionally consistent across all five nodes.

1402 **Resistance shifts become uniformly negative.** At $K = 100,000$, all five nodes show
 1403 negative Δr_i (range: -0.002 to -0.009; mean -0.005), in contrast to the mixed signal
 1404 at $K = 5,000$ (three positive, one negative, one near-zero). With 100,000 individuals
 1405 per node, the effective population size is large enough to suppress drift, revealing that
 1406 the net selection coefficient on resistance is slightly negative under the current parame-
 1407 terization. This likely reflects the cost structure: resistance reduces infection probability
 1408 multiplicatively ($p_{\text{inf}} \propto 1 - r_i$), but the per-locus effect is small with 17 loci ($\Delta p_{\text{inf}} \approx 0.003$

1409 per locus), while background environmental pathogen pressure (P_{env}) ensures continued
1410 exposure regardless of individual resistance.

1411 **Recovery dominance is amplified at scale.** The trait evolution hierarchy becomes
1412 more pronounced at large N : recovery ($\overline{\Delta c_i} = +0.063$) is $13.3\times$ faster than resistance
1413 ($|\overline{\Delta r_i}| = 0.005$) and $12.2\times$ faster than tolerance ($\overline{\Delta t_i} = +0.005$), compared to $4.5\times$ and
1414 $5.0\times$ respectively at $K = 5,000$. The ratio increase occurs because drift no longer inflates
1415 $|\Delta r_i|$ at large N , exposing the true (weak) directional signal on resistance.

1416 **Monterey remains anomalous.** Even at $K = 100,000$, Monterey shows the low-
1417 est crash percentage (97.1% vs. 99.3–99.4% for other nodes), the highest final population
1418 (2,904), the most recoveries (1,319), and the strongest recovery evolution ($\Delta c_i = +0.075$).
1419 This is not a small- N artifact but an emergent property of Monterey’s warmer temper-
1420 atures, which simultaneously drive higher disease pressure *and* stronger selection for
1421 clearance ability.

1422 8.3 Cross-Scale Comparison

1423 Table 15 summarizes the comparison between the two population scales, revealing which
1424 patterns are scale-invariant (and therefore robust model predictions) versus scale-dependent
1425 (and therefore artifacts or emergent threshold effects).

Table 15: Cross-scale comparison of key metrics between $K = 5,000$ and $K = 100,000$ validation runs. “Ratio” column gives the 100K value divided by the 5K value.

Metric	$K = 5\text{K}$	$K = 100\text{K}$	Ratio
Total crash (%)	98.5	98.9	1.004
Mean Δr_i	+0.015	-0.005	—
Mean Δt_i	+0.014	+0.005	0.38
Mean Δc_i	+0.070	+0.063	0.90
Total recoveries	365	4,945	13.5
Monterey crash (%)	99.2	97.1	0.979
Monterey Δc_i	+0.154	+0.075	0.49
Runtime (s)	108	2,558	23.7

1426 Three categories of behavior emerge:

1427 1. **Scale-invariant patterns** (robust predictions):

- 1428 • Population crashes are catastrophic (>97%) at both scales, with no recovery
1429 to pre-epidemic levels.

- Recovery (c_i) is the fastest-evolving trait at every node and both scales.
- Monterey is consistently the most resilient node.
- The extinction vortex—positive feedback between small population size, Allee effects, and continued pathogen pressure—operates at both scales.

2. Scale-sensitive patterns (require caution):

- Resistance evolution: positive at $K = 5,000$ (mean +0.015), negative at $K = 100,000$ (mean -0.005). The sign reversal indicates that drift inflates apparent resistance selection at small N ; the true signal may be negligible or slightly negative.
- Monterey's recovery evolution is 2× stronger at small N ($\Delta c_i = +0.154$ vs. +0.075), suggesting that founder effects amplify trait shifts in small surviving populations.
- Tolerance shifts shrink from +0.014 to +0.005, confirming conditional neutrality.

3. Scale-revealing patterns (insights from large N):

- Uniformly negative Δr_i at $K = 100,000$ reveals that 17 loci provide insufficient genetic variance for resistance evolution to outpace pathogen pressure, consistent with the sensitivity analysis finding that `n_resistance` is the 5th most important parameter (Section 7).
- The crash percentage *increases* at larger N , demonstrating that stochastic rescue is not a viable recovery mechanism and that demographic rescue through immigration or captive breeding is required.

8.4 Key Scientific Findings

The validation runs, taken together with the four-round sensitivity analysis (Section 7), yield several findings with direct implications for conservation management and evolutionary theory.

8.4.1 Evolutionary Rescue Is Insufficient

The central question motivating SSWD-EvoEpi is whether natural selection on polygenic resistance can drive population recovery following the SSWD pandemic. Our results provide a clear negative answer under current parameterization: even over 20 years (~4 generations for *Pycnopodia helianthoides*), evolved resistance produces negligible demographic benefit. At $K = 100,000$, resistance *declines* at all nodes despite ongoing selection against susceptible individuals. Two mechanisms explain this failure:

1463 1. **Insufficient genetic architecture.** With only 17 resistance loci, the maximum re-
1464 sistance score achievable by selection is constrained. Per-locus allele frequency shifts
1465 of ~ 0.001 – 0.003 per generation are an order of magnitude below the $\Delta q \approx 0.08$ – 0.15
1466 reported by Schiebelhut et al. [54] for SSWD-associated loci in *Pisaster ochraceus*.
1467 This discrepancy may reflect either a true species difference or an indication that
1468 more loci of larger effect contribute to resistance in nature than are modeled here.

1469 2. **Environmental pathogen reservoir.** The background environmental pathogen
1470 concentration (P_{env}) ensures continued disease exposure regardless of evolved host
1471 resistance. Even if a subpopulation achieves high mean resistance, P_{env} maintains
1472 baseline infection rates that prevent population recovery below the Allee threshold.
1473 The sensitivity analysis identified $P_{\text{env},\text{max}}$ as the 4th most influential parameter
1474 globally, and the most influential for spatial protection metrics.

1475 This finding is consistent with evolutionary rescue theory [10], which predicts that
1476 rescue is most likely when standing genetic variance is high, generation times are short
1477 relative to population decline rates, and the environment permits population persistence
1478 long enough for adaptation to occur. For *Pycnopodia helianthoides*, with generation times
1479 of ~ 5 years and crash timescales of ~ 2 years, the mismatch is severe.

1480 8.4.2 Recovery as the Primary Adaptive Pathway

1481 The consistent dominance of recovery evolution (c_i) across both scales and all five nodes
1482 suggests that pathogen clearance, rather than infection prevention (resistance) or dam-
1483 age limitation (tolerance), is the primary adaptive pathway available to *P. helianthoides*
1484 under SSWD. This is mechanistically intuitive: recovery acts directly on the transition
1485 probability from infected to recovered state ($p_{\text{rec}} = \rho_{\text{rec}} \times c_i$), creating strong phenotype–
1486 fitness mapping. Individuals that clear infection survive and reproduce; those that do
1487 not, die. The fitness gradient is steep and unambiguous.

1488 However, the absolute recovery trait values remain low even after 20 years of evolution
1489 (final $\bar{c}_i \approx 0.07$ – 0.09 at $K = 100,000$), corresponding to daily clearance probabilities of
1490 only 0.35–0.45% ($p_{\text{rec}} = 0.05 \times c_i$). While selection detectably increases c_i , the result-
1491 ing clearance rates are far below what is needed to substantially reduce disease-induced
1492 mortality.

1493 8.4.3 The Extinction Vortex Persists at Realistic Scales

1494 The persistence of $>97\%$ population crashes at $K = 100,000$ demonstrates that the
1495 extinction vortex identified in the original prototype is not an artifact of small population
1496 sizes. Three reinforcing feedbacks maintain the vortex:

- 1497 1. **Density-dependent transmission:** as the population declines, per-capita con-
 1498 tact rates remain high because pathogen concentration (P_{env}) does not decline pro-
 1499 portionally.
- 1500 2. **Allee effects in reproduction:** below critical densities, broadcast-spawning fer-
 1501 tilization success collapses due to sperm dilution [16], reducing recruitment even
 1502 when surviving individuals are genetically resistant.
- 1503 3. **Sweepstakes reproductive success:** SRS amplifies drift and further reduces N_e
 1504 relative to census N , diminishing the efficacy of selection [25].

1505 The monotonic population decline with no recovery inflection point is consistent with
 1506 field observations: seven years after the initial 2013–2015 pandemic, *P. helianthoides*
 1507 remains functionally absent from most of its former range [18, 22], with only scattered
 1508 observations of wild individuals in California since 2025 [57].

1509 8.4.4 Implications for Captive Breeding

- 1510 The model results strongly reinforce the case for captive breeding and managed release
 1511 as the primary conservation strategy for *P. helianthoides* [5, 33]. Three specific model
 1512 predictions support this conclusion:
- 1513 1. **No natural recovery trajectory exists:** at no node and at no population scale
 1514 does the model predict recovery to >5% of carrying capacity within 20 years. With-
 1515 out demographic intervention, populations remain in the extinction vortex.
- 1516 2. **Recovery trait evolution is the most promising pathway:** if captive breeding
 1517 programs can select for high c_i (pathogen clearance ability), released individuals
 1518 may have elevated survival probability in endemic disease environments. The strong
 1519 fitness gradient on c_i suggests that any heritable variation in clearance ability will
 1520 be rapidly amplified by natural selection post-release.
- 1521 3. **Scale matters:** the worse-at-larger- N result implies that releasing large numbers
 1522 of individuals is necessary but not sufficient; releases must also achieve densities
 1523 above the Allee threshold at the local scale to enable reproductive success.

1524 These predictions align with early empirical results from the Sunflower Star Labora-
 1525 tory, whose December 2025 pilot outplanting achieved 98% survival (47 of 48 juveniles)
 1526 over four weeks at Monterey Bay [57]—the same node that shows the highest resilience
 1527 in our simulations.

1528 **9 Discussion**

1529 **References**

- 1530 [1] Emilius A. Aalto, Kevin D. Lafferty, Susanne H. Sokolow, Richard E. Grewelle,
1531 Tal Ben-Horin, Charles A. Boch, Peter T. Raimondi, Steven J. Bograd, Elliott L.
1532 Hazen, Michael G. Jacox, Fiorenza Micheli, and Giulio A. De Leo. Models with
1533 environmental drivers offer a plausible mechanism for the rapid spread of infectious
1534 disease outbreaks in marine organisms. *Scientific Reports*, 10:5975, 2020. doi: 10.
1535 1038/s41598-020-62118-4.
- 1536 [2] Citlalli A. Aquino, Ryan M. Besemer, Christopher M. DeRito, Jan Kocian, Ian R.
1537 Porter, Peter T. Raiber, John E. Episale, and Ian Hewson. Evidence that microor-
1538 ganisms at the animal-water interface drive sea star wasting disease. *Frontiers in*
1539 *Microbiology*, 11:610009, 2021. doi: 10.3389/fmicb.2020.610009.
- 1540 [3] Einar Árnason, Jere Koskela, Katrín Halldórsdóttir, and Bjarki Eldon. Sweepstakes
1541 reproductive success via pervasive and recurrent selective sweeps. *eLife*, 12:e80781,
1542 2023. doi: 10.7554/eLife.80781.
- 1543 [4] Jorge Arroyo-Esquivel, Alyssa Gehman, Katie Collins, and Fernanda Sanchez. Man-
1544 aging populations after a disease outbreak: exploration of epidemiological con-
1545 sequences of managed host reintroduction following disease-driven host decline.
1546 *bioRxiv*, 2025. doi: 10.1101/2025.02.28.640833.
- 1547 [5] AZA SAFE. Sunflower sea star program plan 2024–2027. Technical report, Associa-
1548 tion of Zoos and Aquariums, 2024.
- 1549 [6] Jenn M. Burt, M. Tim Tinker, Daniel K. Okamoto, Kyle W. Demes, Katie Holmes,
1550 and Anne K. Salomon. Sudden collapse of a mesopredator reveals its complementary
1551 role in mediating rocky reef regime shifts. *Proceedings of the Royal Society B*, 285:
1552 20180553, 2018. doi: 10.1098/rspb.2018.0553.
- 1553 [7] California Ocean Protection Council. Staff recommendation item 9: Consideration
1554 and approval of disbursement of funds to support sunflower sea star reintroduction.
1555 Technical report, California Ocean Protection Council, 2025.
- 1556 [8] Francesca Campolongo, Jessica Cariboni, and Andrea Saltelli. An effective screening
1557 design for sensitivity analysis of large models. *Environmental Modelling & Software*,
1558 22(10):1509–1518, 2007. doi: 10.1016/j.envsoft.2006.10.004.
- 1559 [9] Matthew Clement, Rodrigo Hamede, Menna E. Jones, and Paul A. Hohenlohe.
1560 Coevolution enables host persistence in an eco-evolutionary epidemiological model

- 1561 of Tasmanian devil facial tumor disease. *Evolution*, 78(12):2095–2110, 2024. doi:
1562 10.1093/evolut/qpae143.
- 1563 [10] Matthew Clement et al. Eco-evolutionary individual-based model for coevolution
1564 between Tasmanian devils and devil facial tumour disease. *Evolution*, 2024. doi:
1565 10.1093/evolut/qpae143.
- 1566 [11] Donald L. DeAngelis and Wolf M. Mooij. Individual-based modeling of ecological
1567 and evolutionary processes. *Annual Review of Ecology, Evolution, and Systematics*,
1568 36:147–168, 2005. doi: 10.1146/annurev.ecolsys.36.102003.152644.
- 1569 [12] Michael L. Dungan, Thomas E. Miller, and Donald A. Thomson. Catastrophic
1570 decline of a top carnivore in the Gulf of California rocky intertidal zone. *Science*,
1571 216:989–991, 1982. doi: 10.1126/science.216.4549.989.
- 1572 [13] Morgan E. Eisenlord, Maya L. Groner, Robin M. Yoshioka, Jennifer Elliott, Jeffrey
1573 Maynard, Steven Fradkin, Margaret Turner, Katie Pyne, Sandy Wyllie-Echeverria,
1574 Benjamin G. Miner, and C. Drew Harvell. Ochre star mortality during the 2014
1575 wasting disease epizootic: role of population size and temperature. *Philosophical
1576 Transactions of the Royal Society B*, 371(1689):20150212, 2016. doi: 10.1098/rstb.
1577 2015.0212.
- 1578 [14] Bjarki Eldon and Wolfgang Stephan. Sweepstakes reproduction facilitates rapid
1579 adaptation in highly fecund populations. *Molecular Ecology*, 33:e16903, 2024. doi:
1580 10.1111/mec.16903.
- 1581 [15] Aaron W. E. Galloway, Sarah A. Gravem, Jenna N. Kobelt, et al. Sunflower sea
1582 star predation on urchins can facilitate kelp forest recovery. *Proceedings of the Royal
1583 Society B*, 290:20221897, 2023. doi: 10.1098/rspb.2022.1897.
- 1584 [16] Joanna C. Gascoigne and Romuald N. Lipcius. Allee effects in marine systems.
1585 *Marine Ecology Progress Series*, 269:49–59, 2004. doi: 10.3354/meps269049.
- 1586 [17] Àlex Giménez-Romero, Antoni Grau, Iris E. Hendriks, and Manuel A. Matías. Mod-
1587 elling parasite-produced marine diseases: The case of the mass mortality event of
1588 *Pinna nobilis*. *Ecological Modelling*, 459:109740, 2021. doi: 10.1016/j.ecolmodel.
1589 2021.109740.
- 1590 [18] Sarah A. Gravem and Bruce A. Menge. Metapopulation-scale resilience to disease-
1591 induced mass mortality in a keystone predator: From stasis to instability. *Ecosphere*,
1592 16:e70426, 2025. doi: 10.1002/ecs2.70426.
- 1593 [19] Sarah A. Gravem, Walter N. Heady, Vienna R. Saccomanno, Kathleen F. Alvstad,
1594 Alyssa-Lois M. Gehman, Taylor N. Frierson, and Scott L. Hamilton. *Pycnopodia*

- 1595 *helianthoides*. *The IUCN Red List of Threatened Species*, 2021. doi: 10.2305/IUCN.
1596 UK.2021-1.RLTS.T178290276A197818455.en.
- 1597 [20] Volker Grimm and Steven F. Railsback. *Individual-Based Modeling and Ecology*.
1598 Princeton University Press, Princeton, NJ, 2005.
- 1599 [21] Mary Hagedorn et al. Assisted gene flow using cryopreserved sperm in critically en-
1600 dangered coral. *Proceedings of the National Academy of Sciences*, 118:e2110559118,
1601 2021. doi: 10.1073/pnas.2110559118.
- 1602 [22] Scott L. Hamilton et al. Disease-driven mass mortality event leads to widespread
1603 extirpation and variable recovery potential of a marine predator across the eastern
1604 Pacific. *Proceedings of the Royal Society B*, 288:20211195, 2021. doi: 10.1098/rspb.
1605 2021.1195.
- 1606 [23] C. Drew Harvell, Diego Montecino-Latorre, Joseph M. Caldwell, Jenn M. Burt,
1607 Kathryn Bosley, et al. Disease epidemic and a marine heat wave are associated
1608 with the continental-scale collapse of a pivotal predator (*Pycnopodia helianthoides*).
1609 *Science Advances*, 5:eaau7042, 2019. doi: 10.1126/sciadv.aau7042.
- 1610 [24] Walter N. Heady, Rodrigo Beas-Luna, Michael N. Dawson, et al. Roadmap to re-
1611 covery for the sunflower sea star along the West Coast of North America. Technical
1612 report, The Nature Conservancy, 2022.
- 1613 [25] Dennis Hedgecock and Alexander I. Pudovkin. Sweepstakes reproductive success
1614 in highly fecund marine fish and shellfish: A review and commentary. *Bulletin of*
1615 *Marine Science*, 87:971–1002, 2011. doi: 10.5343/bms.2010.1051.
- 1616 [26] Jon Herman and Will Usher. SALib: An open-source Python library for sensitivity
1617 analysis. *Journal of Open Source Software*, 2(9):97, 2017. doi: 10.21105/joss.00097.
- 1618 [27] Ian Hewson. Microbial respiration in the asteroid diffusive boundary layer influenced
1619 sea star wasting disease during the 2013–2014 northeast Pacific Ocean mass mortality
1620 event. *Marine Ecology Progress Series*, 668:231–237, 2021. doi: 10.3354/meps13710.
- 1621 [28] Ian Hewson. When bacteria meet many arms: Autecological insights into *Vibrio*
1622 *pectinicida* FHCF-3 in echinoderms. *bioRxiv*, 2025. doi: 10.1101/2025.08.15.670479.
- 1623 [29] Ian Hewson, Jason B. Button, Brent M. Gudenkauf, et al. Densovirus associated with
1624 sea-star wasting disease and mass mortality. *Proceedings of the National Academy*
1625 *of Sciences*, 111:17278–17283, 2014. doi: 10.1073/pnas.1416625111.
- 1626 [30] Ian Hewson, Morgan R. Johnson, and Benjamin Reyes-Chavez. Lessons learned
1627 from the sea star wasting disease investigation. *Annual Review of Marine Science*,
1628 17:257–279, 2025. doi: 10.1146/annurev-marine-040623-082617.

- 1629 [31] Ian Hewson et al. Investigating the complex association between viral ecology, envi-
1630 ronment, and Northeast Pacific sea star wasting. *Frontiers in Marine Science*, 5:77,
1631 2018. doi: 10.3389/fmars.2018.00077.
- 1632 [32] Ian Hewson et al. Perspective: Something old, something new? Review of wasting
1633 and other mortality in Asteroidea (Echinodermata). *Frontiers in Marine Science*, 6:
1634 406, 2019. doi: 10.3389/fmars.2019.00406.
- 1635 [33] Jason Hodin, Amanda Pearson-Lund, Freya P. Anteau, Philippe Kitaeff, and Sarah
1636 Cefalu. Progress toward complete life-cycle culturing of the endangered sunflower
1637 star, *Pycnopodia helianthoides*. *Biological Bulletin*, 241:243–258, 2021. doi: 10.1086/
1638 716552.
- 1639 [34] Ilse Höllinger, Pleuni S. Pennings, and Joachim Hermissen. Polygenic adaptation:
1640 From sweeps to subtle frequency shifts. *eLife*, 11:e66697, 2022. doi: 10.7554/eLife.
1641 66697.
- 1642 [35] C. Lambert, J.-L. Nicolas, V. Cilia, and S. Corre. *Vibrio pectenicida* sp. nov., a
1643 pathogen of scallop (*Pecten maximus*) larvae. *International Journal of Systematic
1644 Bacteriology*, 48:481–487, 1998. doi: 10.1099/00207713-48-2-481.
- 1645 [36] Ryan E. Langendorf, James A. Estes, James C. Watson, Michael C. Kenner, Brian B.
1646 Hatfield, M. Tim Tinker, Elizabeth Waddle, Michelle L. DeMarch, and Daniel F.
1647 Doak. Dynamic and context-dependent keystone species effects in kelp forests. *Pro-
1648 ceedings of the National Academy of Sciences*, 2025. doi: 10.1073/pnas.XXXXXXX.
- 1649 [37] Harilaos A. Lessios. The great *Diadema antillarum* die-off: 30 years
1650 later. *Annual Review of Marine Science*, 8:267–283, 2016. doi: 10.1146/
1651 annurev-marine-122414-033857.
- 1652 [38] Katie E. Lotterhos and Michael C. Whitlock. The relative power of genome scans to
1653 detect local adaptation depends on sampling design and statistical method. *Molec-
1654 lar Ecology*, 24(5):1031–1046, 2015. doi: 10.1111/mec.13100.
- 1655 [39] Dayv Lowry, Sarah Wright, Melissa Neuman, et al. Endangered Species Act status
1656 review report: Sunflower sea star (*Pycnopodia helianthoides*). Technical report,
1657 NOAA National Marine Fisheries Service, 2022.
- 1658 [40] Carolyn J. Lundquist and Louis W. Botsford. Model projections of the fishery
1659 implications of the Allee effect in broadcast spawners. *Ecological Applications*, 14:
1660 929–941, 2004. doi: 10.1890/02-5325.

- 1661 [41] Coralie Lupo, Pedro J. Cabello-Yeves, Sara Ferreira, Julien de Lorgeril, and Luigi
1662 Vezzulli. Vibrio ecology, pathogenesis, and evolution. *Frontiers in Microbiology*, 11:
1663 587685, 2020. doi: 10.3389/fmicb.2020.587685.
- 1664 [42] Coralie Lupo et al. Spatial epidemiological modelling of infection by *Vibrio aestuari-*
1665 *anus* shows that connectivity and temperature control oyster mortality. *Aquaculture*
1666 *Environment Interactions*, 12:511–527, 2020. doi: 10.3354/aei00379.
- 1667 [43] Michael Lynch. Evolution of the mutation rate. *Trends in Genetics*, 26:345–352,
1668 2010. doi: 10.1016/j.tig.2010.05.003.
- 1669 [44] Ryan T. Mancuso, Sarah A. Gravem, Rachel S. Campbell, Nathan Hunter, Pete
1670 Raimondi, Aaron W. E. Galloway, and Kristy J. Kroeker. Sunflower sea star chemical
1671 cues locally reduce kelp consumption by eliciting a flee response in red sea urchins.
1672 *Proceedings of the Royal Society B*, 2025. doi: 10.1098/rspb.2025.0949.
- 1673 [45] Zofia D. Meunier, Sally D. Hacker, and Bruce A. Menge. Regime shifts in rocky
1674 intertidal communities associated with a marine heatwave and disease outbreak.
1675 *Nature Ecology & Evolution*, 8:1285–1297, 2024. doi: 10.1038/s41559-024-02425-5.
- 1676 [46] C. Melissa Miner, Jennifer L. Burnaford, Richard F. Ambrose, Liam Antrim, et al.
1677 Large-scale impacts of sea star wasting disease (SSWD) on intertidal sea stars and
1678 implications for recovery. *PLoS ONE*, 13:e0192870, 2018. doi: 10.1371/journal.pone.
1679 0192870.
- 1680 [47] Diego Montecino-Latorre, Morgan E. Eisenlord, Morgan Turner, Reyn Yoshioka,
1681 C. Drew Harvell, et al. Devastating transboundary impacts of sea star wasting
1682 disease on subtidal asteroids. *PLoS ONE*, 11:e0163190, 2016. doi: 10.1371/journal.
1683 pone.0163190.
- 1684 [48] Max D. Morris. Factorial sampling plans for preliminary computational experiments.
1685 *Technometrics*, 33(2):161–174, 1991. doi: 10.1080/00401706.1991.10484804.
- 1686 [49] Maya B. Prentice, Citlalli A. Aquino, Amy M. Chan, Kalia M. Davis, Paul K. Her-
1687 shberger, Jan F. Finke, Jason Hodin, Aquiala McCracken, Christina T. E. Kellogg,
1688 Rute B. G. Clemente-Carvalho, Christy Prentice, Kiana X. Zhong, C. Drew Harvell,
1689 Curtis A. Suttle, and Alyssa-Lois M. Gehman. *Vibrio pectenicida* strain FHCF-3 is
1690 a causative agent of sea star wasting disease. *Nature Ecology & Evolution*, 2025. doi:
1691 10.1038/s41559-025-02797-2.
- 1692 [50] Lars Råberg, Andrea L. Graham, and Andrew F. Read. Decomposing health: toler-
1693 ance and resistance to parasites in animals. *Philosophical Transactions of the Royal*
1694 *Society B*, 364(1513):37–49, 2009. doi: 10.1098/rstb.2008.0184.

- 1695 [51] Laura Rogers-Bennett and Cynthia A. Catton. Marine heat wave and multiple
1696 stressors tip bull kelp forest to sea urchin barrens. *Scientific Reports*, 9:15050, 2019.
1697 doi: 10.1038/s41598-019-51114-y.
- 1698 [52] Andrea Saltelli. Making best use of model evaluations to compute sensitivity in-
1699 dices. *Computer Physics Communications*, 145(2):280–297, 2002. doi: 10.1016/
1700 S0010-4655(02)00280-1.
- 1701 [53] Andrea Saltelli, Marco Ratto, Terry Andres, Francesca Campolongo, Jessica Cari-
1702 boni, Debora Gatelli, Michaela Saisana, and Stefano Tarantola. *Global Sensitivity*
1703 *Analysis: The Primer*. John Wiley & Sons, 2008. doi: 10.1002/9780470725184.
- 1704 [54] Lauren M. Schiebelhut, Jonathan B. Puritz, and Michael N. Dawson. Decimation
1705 by sea star wasting disease and rapid genetic change in a keystone species, *Pisaster*
1706 *ochraceus*. *Proceedings of the National Academy of Sciences*, 115:7069–7074, 2018.
1707 doi: 10.1073/pnas.1800285115.
- 1708 [55] Lauren M. Schiebelhut, Jonathan B. Puritz, and Michael N. Dawson. Decimation
1709 by sea star wasting disease and rapid genetic change in a keystone species, *Pisaster*
1710 *ochraceus*. *Proceedings of the National Academy of Sciences*, 115(27):7069–7074,
1711 2018. doi: 10.1073/pnas.1800285115.
- 1712 [56] Lauren M. Schiebelhut et al. A reference genome for ecological restoration of the
1713 sunflower sea star, *Pycnopodia helianthoides*. *Journal of Heredity*, 115:86–93, 2024.
1714 doi: 10.1093/jhered/esad054.
- 1715 [57] Sea Star Lab. Sea star cryopreservation breakthrough inspires hope for sunflower
1716 stars, 2025. Press release.
- 1717 [58] Il'ya M. Sobol'. Global sensitivity indices for nonlinear mathematical models and
1718 their Monte Carlo estimates. *Mathematics and Computers in Simulation*, 55(1–3):
1719 271–280, 2001. doi: 10.1016/S0378-4754(00)00270-6.
- 1720 [59] Sunflower Star Lab. First-ever temporary experimental outplanting of sunflower
1721 stars in California, 2025. Press release.
- 1722 [60] Nick Tolimieri. Appendix A: Population viability analysis of *Pycnopodia he-*
1723 *lianthesoides*. In: Lowry et al., *ESA Status Review Report, NOAA NMFS*, 2022.
- 1724 [61] David L. J. Vendrami, Lloyd S. Peck, Melody S. Clark, Bjarki Eldon, Michael Mered-
1725 ith, and Joseph I. Hoffman. Sweepstake reproductive success and collective dispersal
1726 produce chaotic genetic patchiness in a broadcast spawner. *Science Advances*, 7:
1727 eabj4713, 2021. doi: 10.1126/sciadv.abj4713.

- 1728 [62] John P. Wares and Lauren M. Schiebelhut. What doesn't kill them makes them
1729 stronger: an association between elongation factor 1- α overdominance in the sea
1730 star *Pisaster ochraceus* and "sea star wasting disease". *PeerJ*, 4:e1876, 2016. doi:
1731 10.7717/peerj.1876.
- 1732 [63] Helen J. Wearing, Pejman Rohani, and Matt J. Keeling. Appropriate models for the
1733 management of infectious diseases. *PLoS Medicine*, 2(7):e174, 2005. doi: 10.1371/
1734 journal.pmed.0020174.

1735 **A Parameter Tables**